UNIVERSITY OF CRETE

Spectral and Timing Analysis of Swift J005139.2-721704, a transient Be/X-Ray Pulsar

Undergraduate Thesis

Konstantinos Droudakis A.M 4514

Supervisor: Prof. Andreas Zezas

Department of Physics
Heraklion, 2021

Acknowledgments

I would like to express my gratitude to professor Andreas Zezas for his guidance on this project. His exceptional knowledge assisted me on improving my skills and broadened my horizons on this majestic field called Astrophysics.

I would also like to thank Dr. Pablo Reig for helping with the search of the pulsar’s period and Dr. Konstantinos Kovlakas and Dr. Grigoris Maravelias for the tech support and the helpful discussions we had.

Table of Contents

Chapter 1

Introduction

1.1. Pulsars

Rapidly rotating neutron stars, or as we came to know them, *Pulsars*, are some of the most spectacular objects in the universe. Born out of supernovae, these stellar cores are continually testing our understanding of physics, since we do not have complete understanding as to their structural makeup, nor to the mechanism that produces such powerful magnetic fields that they have.

Pulsars were first detected in 1967 as an almost perfectly regular pulse of radio waves, by Jocelyn Bell Burnell and Antony Hewish using the Interplanetary Scintillation Array in Cambridge, UK, and since then, discoveries regarding their properties keep surprising the scientific community. That year also marked the beginning of a series of discoveries and changes to the fundamental understanding of stellar evolution theories, since a sudden realization that not only neutron stars exist, but they make up a non negligible percentage of stellar bodies in the Milky Way, with today's estimates putting the number of neutron stars in our galaxy around the 1 billion mark (NASA [1]), means that they play an important role in the evolution of the stars in the universe.

A typical neutron star has a radius of 10 km and an average density in the order of 10^{17} kg/m^3, approximating an atomic nuclear density of ~ 2.3×10^{17} kg/m^3. Their masses range from 1.1 $M_\odot$ to 2.16 (Rezzolla, Most and Weih, 2018) (for non rotating neutron stars), an upper limit known as the Tolman–Oppenheimer–Volkoff limit. Beyond that limit, any object collapses into a black hole, since its internal pressure cannot support its mass against its collapse. The magnetic field of a pulsar ranges from 10^4–10^{11} T, or 10^8–10^{15} G (Reisenegger, 2003). For comparison, the Earth's magnetic field is 0.25 – 0.65 G at its surface (Call for Papers: Special Issue of Earth, Planets and Space (EPS) "International Geomagnetic Reference Fieldg - the eleventh generation", 2009). The interior structure of a neutron star is still unclear, although most models agree in a structure such as the one shown in Figure 1.

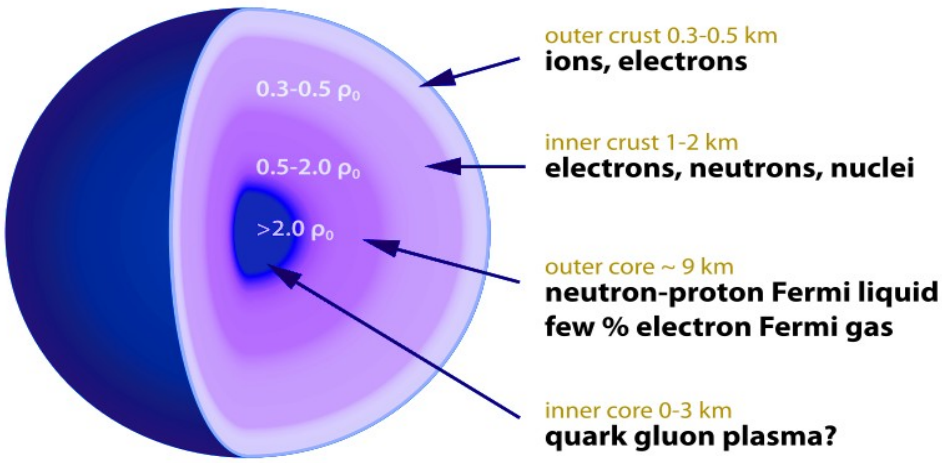

Figure 1: A cross-section of a neutron star, showcasing a theoretical structural makeup of its interior. ρ_0 ~ 10^{-3} fm is the nuclear matter saturation density, which is approximately equal to a nucleus density. (Image credit: Haensel, Potekhin and Yakovlev, 2007) - edited

1 https://www.nasa.gov/mission_pages/GLAST/science/neutron_stars.html

Pulsars are created when a massive star (~ 8 - 20 $M_\odot$) explodes in a supernova at the end of its life and its core collapses. The collapse causes the core to exceed the Chandrasekhar limit and the neutron star to be born. The Chandrasekhar limit is the upper boundary of mass for a white dwarf at which the electron degeneracy pressure barely overcomes the gravitational forces, keeping it stable. The value is calculated to be around 1.4 $M_\odot$, or 2.765×10^{30} kg (Mazzali, Ropke, Benetti and Hillebrandt, 2007). Due to the conservation of angular momentum, a massive star increases its rotational speed while collapsing to form a neutron star. The fact that the change in the radius of the object during this process is so great makes the pulsar acquire rotational periods ranging from seconds to 10^{-2} seconds.

1.2. X-Ray Binaries

An *X-Ray Binary System* is a binary star system consisting of two objects, a donor star and an accretor. The names come from the fact that the orbits of those systems are close enough for matter to leave the donor star and fall onto the accretor in a process called *accretion* (see Section 1.3) and in addition, produce X-rays. The donor can be a main sequence star or an evolved star, while the accretor is a compact object, with a gravitational field strong enough to accelerate matter up to energies in the order of 0.1 to 100 keV, in the X-ray domain. A compact object can be a neutron star, a black hole, or a white dwarf, with each case defining a sub-category (Reig, 2011).

1.2.1. High Mass X-Ray Binaries

A *High Mass X-Ray Binary System (HMXB)* is an X-ray binary system with a massive donor star. HMXBs are a sub-category of X-Ray Binaries together with Low Mass X-Ray Binaries and Intermediate Mass X-Ray Binaries, divided solely based on the donor's mass (or spectral type). Generally, HMXBs have a donor star with spectral type of O, B, or Be, or a blue supergiant. The X-ray spectrum of HMXBs is harder than the other two sub-categories, with photons dominating the domain above 10 keV. In Figure 2 we can see the Hertzsprung–Russell diagram with the ranges of donor stars of HMXBs highlighted with a red ellipse.

1.2.2. Be/X-Ray Binaries

Be/X-Ray Binaries (BeXRBs) are a sub-class of HMXBs where the donor star is a Be star and the accretor is a neutron star. They are a part of 3 sub-categories of HMXBs together with Supergiant X-Ray Binaries (SGXBs) and Supergiant Fast X-ray Transients (SFXTs) (Negueruela et al. 2005).

A Be star is defined as a non-supergiant star B spectral type, that has Balmer emission lines in its spectrum. The Balmer lines are the result of equatorial gaseous disks (circumstellar disks) formed by the star's rapid rotation (Struve, 1931). This disk can be better pictured as the result of a wide atmosphere near the equator, still connected to the star, with the gas density decreasing as we get further in the disk. In a binary pair, the compact object may cross this disk during its orbit, causing matter to accrete directly to it, resulting in an outburst that we can observe.

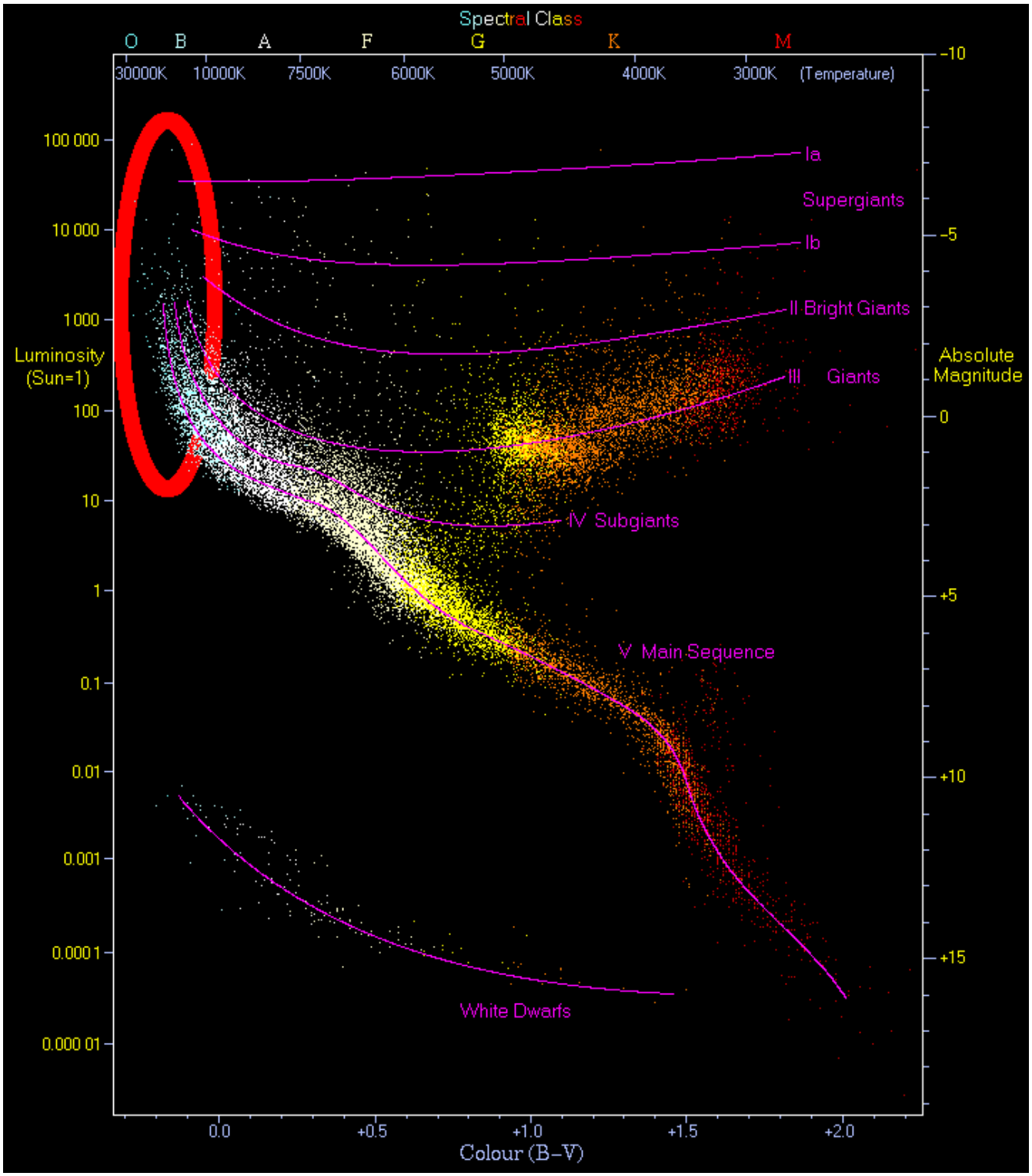

Figure 2: Hertzsprung–Russell diagram (HR Diagram) showcasing (with the red ellipse) the donor stars of HMXBs. (Image credit: Richard Powell with data from Hipparcos and Gliese Catalogue) - edited

1.3. Transient X-Ray Pulsars

A *Transient X-Ray Pulsar* is a pulsar that temporarily becomes a source of X-rays. This can happen for a variety of reasons. Most commonly, the pulsar is a part of a binary system and its orbit is elliptical. This results in two different time periods, when the distance between the two objects of the pair is large, and when it is short enough for matter to be accreted from the donor star to the pulsar. The outburst duration depends on the mass and evolutionary stage of the donor star and their orbital parameters and it usually lasts from a few days to a few weeks, until the gas in the accretion disk that had formed runs out (see *Section 1.4*).

Transient sources, in general, are observed only during their outbursts, and although most of them appear to happen periodically during a periastron passage, that period can take months, or even years to elapse. Using these observations though, we can uncover information about the donor star. A large number of Transient X-Ray Pulsars are in orbit around Be Stars, with their outbursts helping us impose constraints in orbital parameters (such as period eccentricity) and study the accretion process. We can see an example of a Transient X-Ray Pulsar in Figure 3.

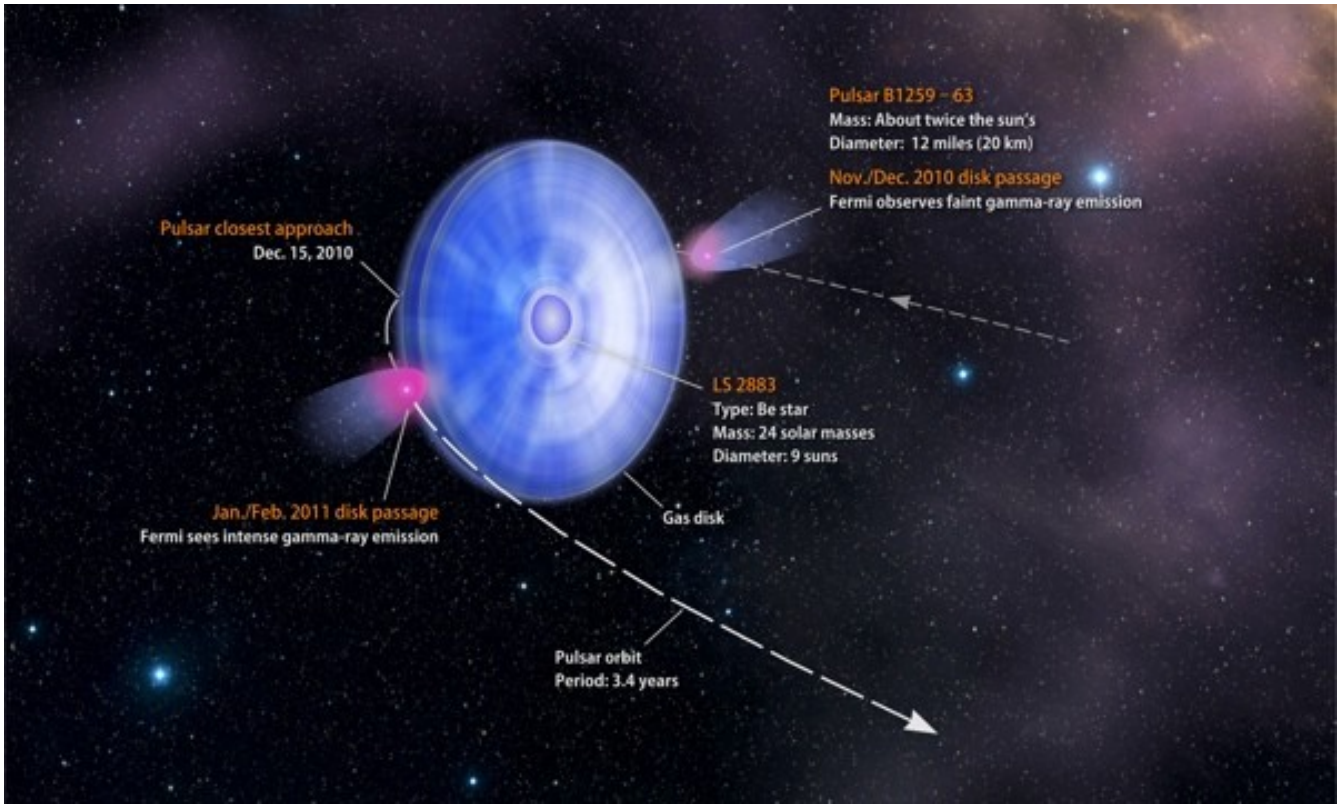

Figure 3: A Be Star – Pulsar pair (LS 2883 with Pulsar B1259-63), showcasing the relation between their orbiting period and the X-ray outbursts. In this example, the first outburst begins in November 2010 and the second one in January 2011, when the pulsar enters the two sides of the disk. After the periastron, the accretion stops for a period of 3.4 years, until the pulsar's orbit brings it closer to its donor star to accrete matter once more. (Image credit: NASA's Goddard Space Flight Center/Francis Reddy)

1.4. Accretion

Accretion is defined as the accumulation of matter (commonly gaseous) onto an object and it is one of the most important processes in our universe. This process alone is responsible for the formation of a wide variety of objects, from planets and asteroids, to entire galaxies. Accretion also allows us to observe objects that where otherwise invisible to our instruments, for example, a pulsar that cannot emit enough light on its own can be transformed into one of the brightest objects in a galaxy due to the matter that is accreted onto it from a donor star, converting the gravitational energy of the gas to pure light.

1.4.1. Types of Accretion in Binaries

In a binary stellar system, accretion has been observed to occur in three different ways:

- Stellar Wind Accretion
- Roche Lobe Accretion
- Be Star Accretion

Stellar wind accretion takes place when the pulsar attracts material from the donor's star stellar wind. Although, generally, the mass that is accreted is not as large as the other two types, stellar wind accretion can still create an outburst that we can observe.

Roche Lobe Accretion is the accretion that occurs when the two objects come close enough for the donor star to fill its Roche lobe. A Roche Lobe is the result of the combined gravitational forces of the pair. The Lagrange point 1 (L1) of the system plays an important role for the formation of its distinct teardrop shape, as it is the point where the Roche lobe of each object connects.

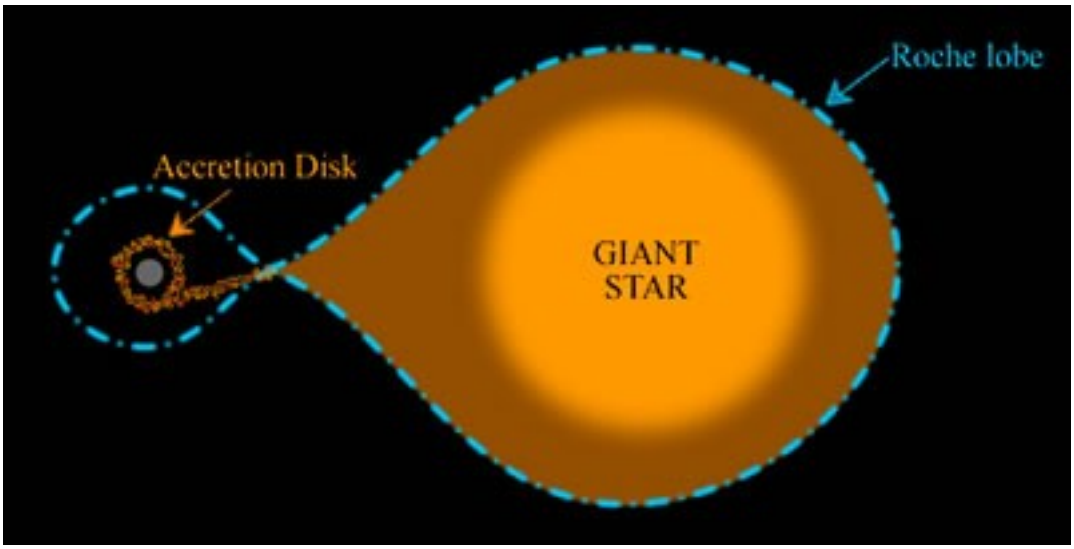

Figure 4: Roche lobe creation between a compact object and a massive stellar companion. The point where the two Roche lobes meet is the Lagrange point 1. (Image credit: https://astronomy.swin.edu.au/cosmos/r/roche-lobe)

By examining Figure 4 we can see that matter originating from the donor star flows through the L1 point to the vicinity of the compact object. As the gas fall in the gravitational potential of the compact object it obtains large velocity, while its rotational velocity increases due to angular momentum conservation. The accumulation of the matter around the compact object creates what we call an *accretion disk*, a structure sharing resemblance with the rings of Saturn, as we can see again in Figure 4.

Finally, the Be star accretion takes place inside of the circumstellar disk of a Be star. If the orbits bring the pair close enough, where the compact object can attract material from the Be-star's circumstellar disk, gas falls directly to the surface of it, as we saw in Figure 3.

1.4.2. Accretion Column

This research project focuses on the structural aspects of the accretion column, so a brief presentation of the basic sources of X-ray photons and the physical processes of matter accretion on the accretion column will follow.

As mentioned before, matter from the stellar companion of the X-ray binary approaches the pulsar, where it creates an accretion disk. The turbulent flow of gas orbiting the neutron star causes collisions between the particles, slowly "draining" the angular momentum of the matter (we could call this process "friction"), resulting in a spiral motion towards the pulsar, until it reaches the lowest possible orbit. This orbit is located on the Alfven Radius, where the magnetic energy density is equal to the kinetic energy density. In the case of neutron stars, the magnetic field is playing a crucial role. Following the magnetic field lines, gas ends up above the poles of the pulsar where it begins its fall towards the surface and because of the intense gravitational pull, it acquires relativistic velocities (see Figure 5). Lower in the accretion column the gas moves with supersonic speeds, forming a standing shock. Below the shock the gas slowly drifts towards the pulsar surface. The accumulated gas at the surface of the neutron star emits thermal radiation, which, in combination with cyclotron and bremsstrahlung radiation processes as well as the scattering of the photons due to collisions with high speed electrons (comptonization), create the final X-ray spectrum we observe (Becker and Wolff, 2007).

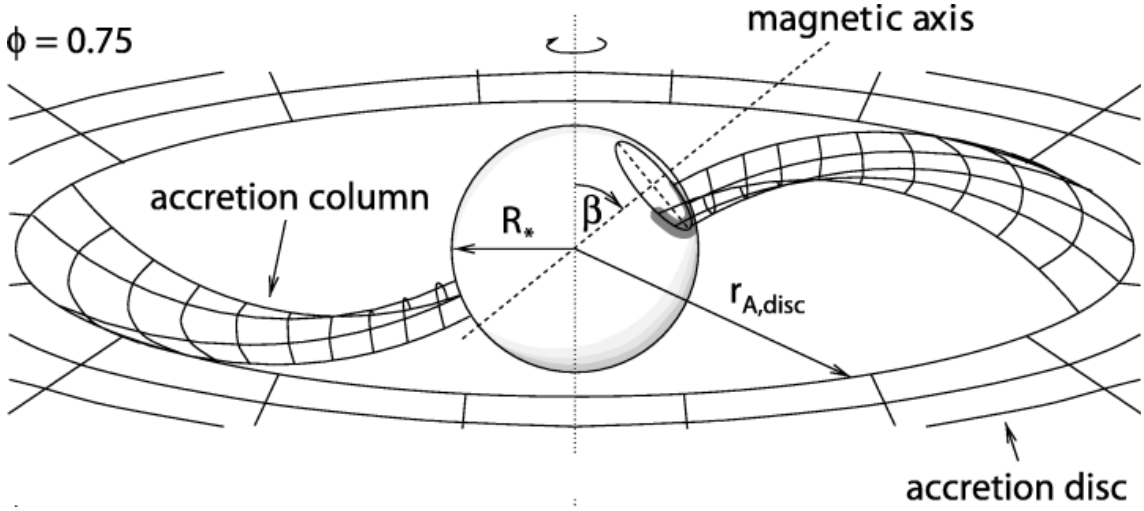

Figure 5: Matter is falling from the accretion disk to the accretion column in a pulsar. (Image credit: Galloway, Giles, Wu and Greenhill, 2001)

In Figure 6 we can see the aforementioned process. The green arrows illustrate the in falling matter and the blue wave-arrows represent the emitted X-rays. The red arrow waves are the thermal photons that cause the spectrum to have a blackbody component. As the pulsar rotates, we expect to observe the accretion column from different angles, so, as we will see in the methodology section, certain features that appear in the spectrum are constant, while others change periodically.

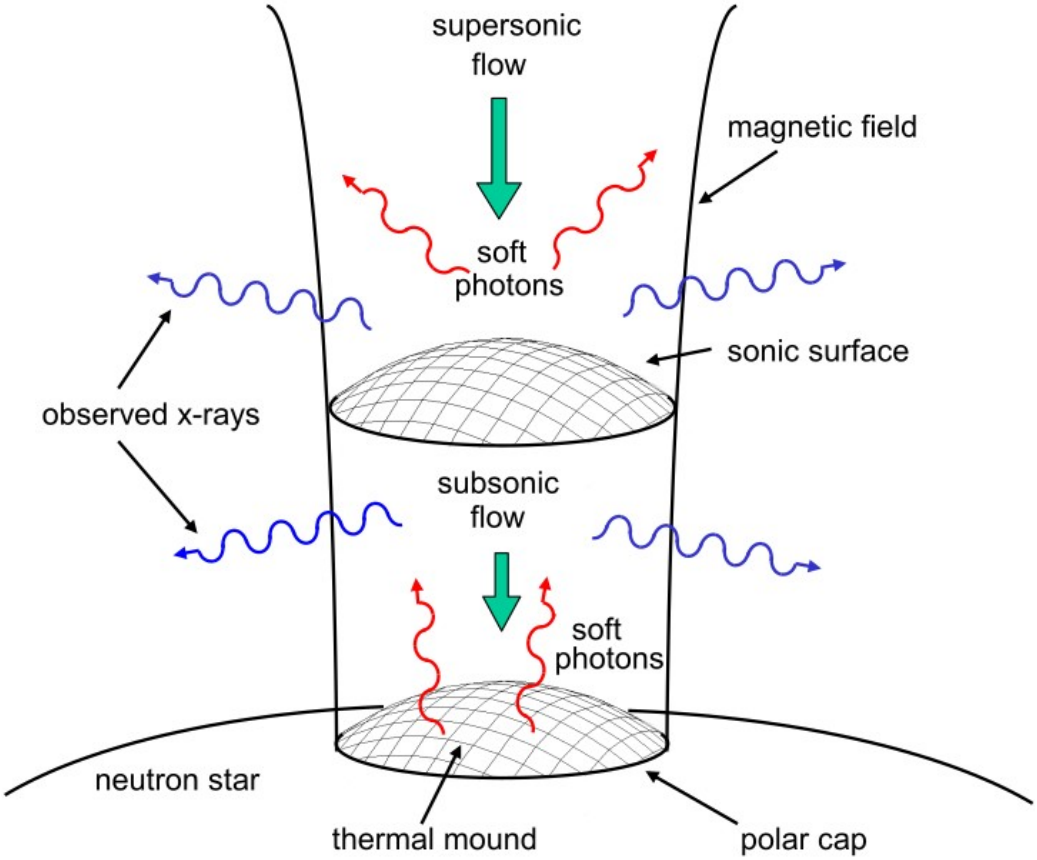

Figure 6: Accretion column of a neutron star and the accreting matter flow on its pole. The produced X-rays are also illustrated (Image credit: Becker and Wolff, 2007)

1.5. Cyclotron Resonant Scattering Features

Cyclotron Resonant Scattering Features (CRSF) are spectral features observed in a number of X-ray binaries in the form of an absorption line, or sequence of lines following a harmonic energy series. The harmonic nature of these lines are caused by the Landau levels. Electrons that reside in the 1st Landau level (~ 20 - 40 keV) collide with high speed protons and get excited to higher levels. When photons get absorbed by those electrons they create absorption lines based on the energy of the electron they collided with. The energy of the fundamental line is given by (e.g. Becker & Wolff 2007)

$$\varepsilon_c = \frac{e\,B\,h}{2\pi\, m_e c} \approx 11.57\, B_{12}\,(keV)$$

where: B_{12} is the magnetic field measured in units of 10^{12} Gauss, or $B_{12} = \frac{B}{10^{12}\,G}$,

c	the speed of light,
h	the Planck's constant,
m_e	the electron's mass,
e	the electron's charge

By using this relation, CRSFs can provide an estimation of the magnetic field of the pulsar. CRSFs can vary from obvious to subtle, as well as over a wide range of energies, depending on the pulsar's magnetic field and the observed harmonic. An example of a prominent CRSF in the binary system RX J0520.5−6932 (Tendulkar et al., 2014) is shown below.

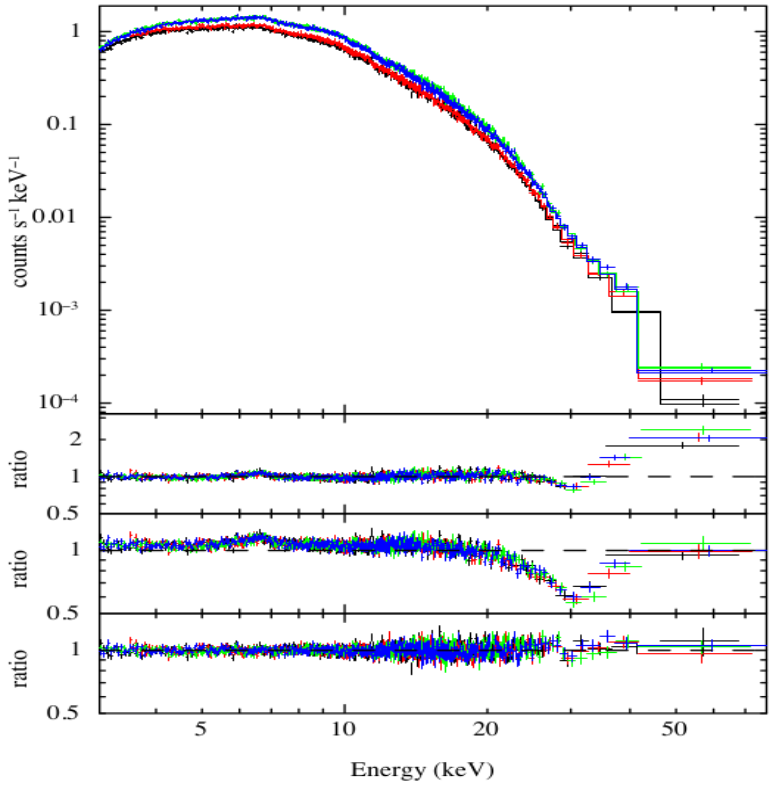

Figure 7: Top panel: X-ray spectrum of the binary RX J0520.5-6932 obtained with the NuSTAR observatory. The colored points show data from 2 detectors (FPMA and FPMB) and 2 observations (Obs1: black for FPMA and red for FPMB, Obs2: green for FPMA and blue for FPMB). The 3 bottom panels show the fit ratios assuming: (a) a power-law model with a Fermi-Dirac cutoff (Tanaka, 1986) with photoelectric absorption; (b) same as (a) with the addition of the cyclotron model described above at ~30 keV and an emission line at 6.5 keV with their line strengths set to 0 and (c) same as (b) with the two lines fitted to the data. (Tendulkar et al., 2014)

As we will discuss later, the 1st feature is an Iron emission line and the 2nd is the cyclotron line (third block from top). In this example, the missing cyclotron component results in very strong residuals at ~30 keV, so the existence of the CRSF is clear. In many other cases, the search for the cyclotron line can be quite challenging, sometimes being observed only in the Phase Resolved Analysis on specific pulse phases of the object in question. This is the reason we need to proceed breaking down the pulse into discrete phases and taking our analysis one step further.

1.6. Purpose of this project

The pulsar we studied gave us a rare chance to observe a source above the Eddington limit. The Eddington Limit (or Eddington Luminosity) is the maximum luminosity that can be radiated by an accretion flow when its radiation pressure is balanced by its gravitational force. Sources exceeding the Eddington limit are expected to eject matter due to their immense radiation. Although this limit was introduced for stars, this definition also applies for accreting sources like X-ray binaries. That means that if the luminosity of an accreting pulsar is above the Eddington limit, matter in the accretion disk will be blown away because of the extreme radiation pressure. Studying these sources can give us insight on the processes that take place in the region of the accretion disk and the accretion column.

In conclusion, the purpose of this project was to study the X-ray spectrum of an X-ray pulsar accreting close and above the Eddington limit. This analysis is performed by applying an appropriate theoretical model that allows us to extract information on the physical conditions within the accretion column. We also explored for spectral variations and physical conditions of the accretion flow within the pulse period i.e. in different pulse phases (phase resolved spectroscopy).

Chapter 2

Observations and Methodology

2.1. NuSTAR

The data we used are observations of the Swift J005139.2-721704 accreting X-ray pulsar and were acquired by the ***Nu***clear ***S***pectroscopic ***T***elescope ***Ar***ray (NuSTAR), an X-ray space-based telescope launched in mid-June 2012. NuSTAR is capable of focusing X-rays of energies in the range of 3 – 79 keV (Harrison et al., 2013) and its launch marked the first time we could extract images and spectra above 10 keV.

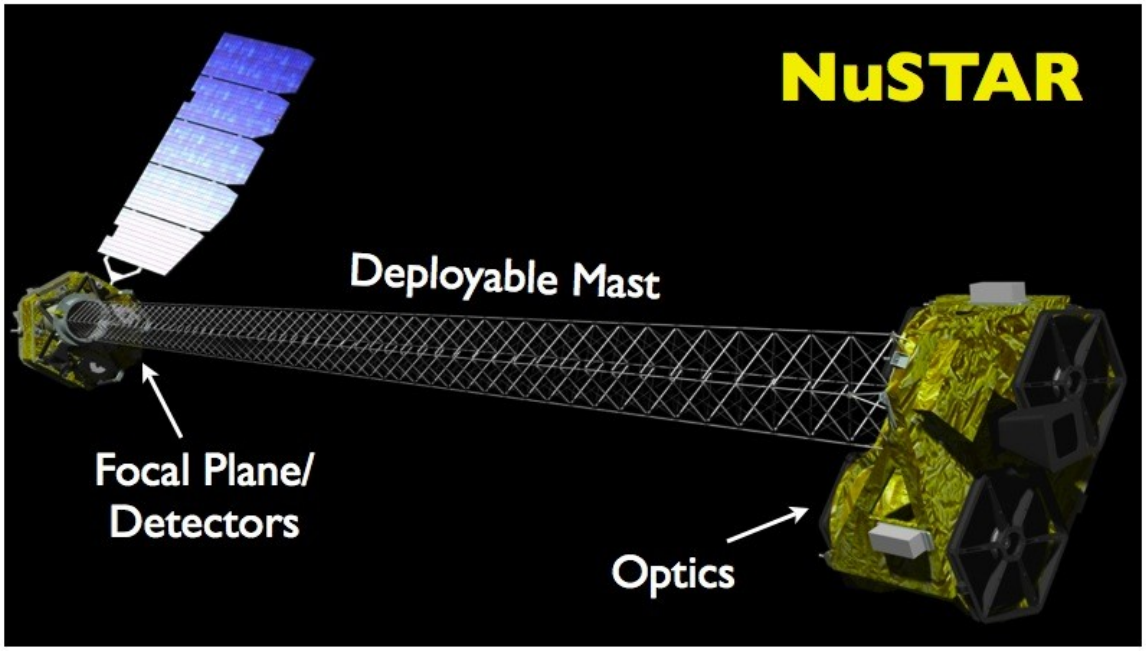

Figure 8: NuSTAR with its major parts pinpointed (Image credit: NASA/HEASARC)

The observatory consists of 2 detectors, FPMA and FPMB, named by their focal plane modules. In Figure 5 above we can see that they lie on the left side, while the optics are placed on the right. Due to design of X-ray mirrors (grazing incidence), the focal length of the telescope is ~10m, requiring a long deployable mast connecting the mirror with the detector module. X-rays cannot be focused with the common reflection methods, due to their high energy that gets absorbed and re-emitted as lower energy photons. A simple illustration that showcases that process is shown in Figure 9. Each detector, laying on the focusing point shown in the image above, is divided into 4 rectangular pieces as shown in Figure 10.

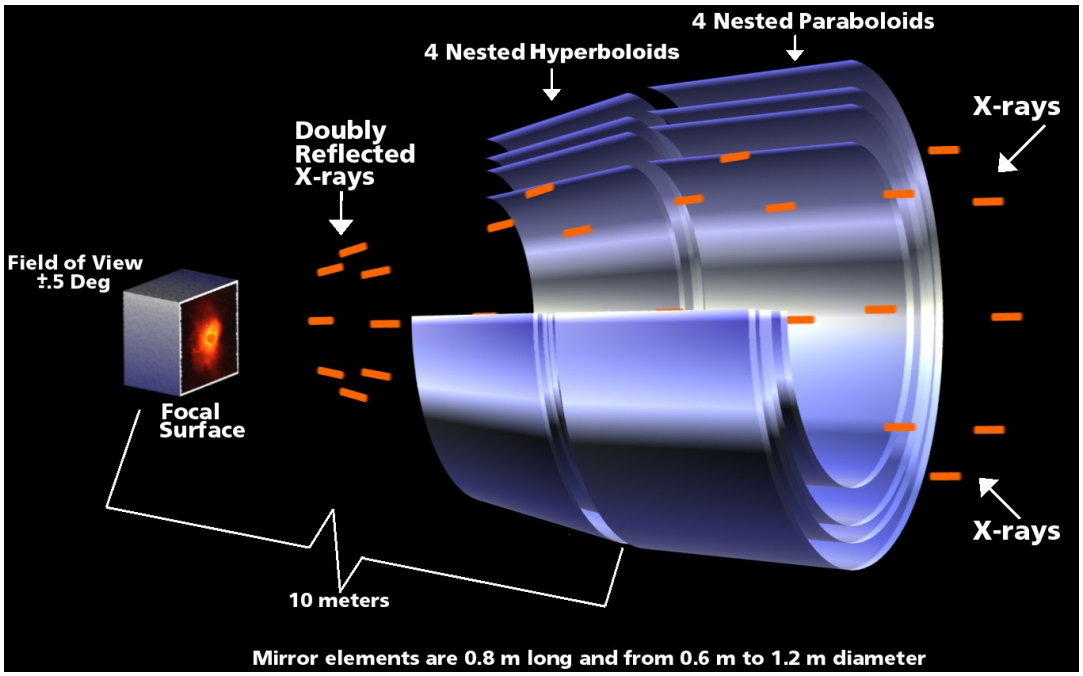

Figure 9: X-ray focusing schematic for Chandra X-Ray Space Observatory (Image credit: NASA/CXC/D.Berry)

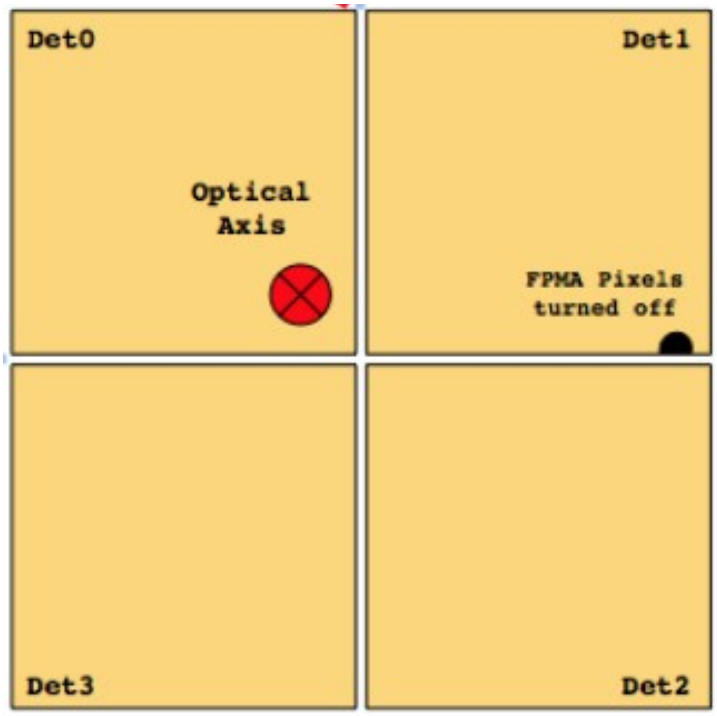

Figure 10: Depiction of the structure of a NuSTAR detector. (image credit: NuSTAR quick-start guide)

2.2. Observations

Swift J005139.2-721704 is observed in 3 occasions following the evolution of its outburst, as we can see on Table 2.1.

Table 2.1
Observational information

OBSERVATION ID	**Observation Date**	**Exposure Time** (ksec.)	**Total Pixel Count** (counts)	**Countrate** (counts/sec.)
30361003002	November 19th 2018	74.5	623788	8.373
30361003004	November 24th 2018	38.2	490679	12.845
30361003006	November 27th 2018	73.2	1036512	14.16

In Figure 11 we can see that the intensity of the source increases with time. This increase reaches a factor of 1.7 in the third observation. This allows us to study the dependence of the X-ray spectrum and the accretion flow on the accretion rate. The counts presented originate only from the source, after the removal of the background.

Countrate – Time Diagram

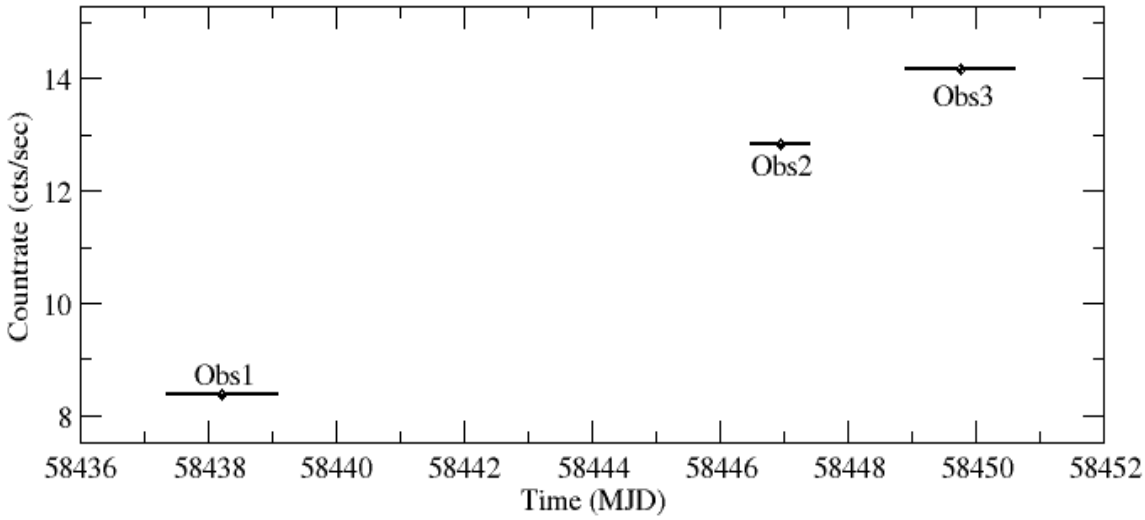

Figure 11: Countrate (counts/second) as a function of time (MJD). The line represents the duration of each observation.

2.3. The Target

The object of our study is classified as a HMXB system of a rapidly spinning neutron star (Pulsar XTE 0052-723 or SXP 4.78) and an OB star ([M2002] SMC 20671 with a specific spectral type of B0.5 IV-V).

The pair was first discovered after observations of the Rossi X-Ray Timing Explorer (RXTE) on December 2000 (Laycock et al. 2002) during its outbursts. Then, on November 19th 2018, an other outburst was spotted lasting for about 12 days, which is the source of the data analyzed on this project. The pulsar spins with a period of 4.78 seconds (Laycock et al. 2002) and it is located in the Small Magellanic Cloud (SMC) at a distance of 60.6 kpc (Hilditch et al. 2004), assuming that the distance to the SMC is significantly larger than its size, so every object that lies in the dwarf galaxy is considered to be at the same distance. In Figure 9 we can see an optical image of the location of SXP 4.78 relative to the SMC.

The SMC and Large Magellanic Cloud (LMC) are considered good targets for observing HMXBs due to their position in the sky. By laying outside of the plane of the Milky Way, both dwarf galaxies are way clearer than any same distance targets inside our galaxy. The lack of galactic dust and gas not only allows more wavelengths of light to reach us, but it also makes our data more reliable. This is partly the reason we observe a high amount of outbursts from pulsars belonging in HMXBs in the SMC.

Figure 12: Optical image of the SMC from SDSS (fov ~ 5^o x 2.7^o) and the location of Swift J005139.2-721704 (SXP 4.78) pinpointed with the cross in the middle.

2.4. Data Analysis

In this subsection we will discuss the steps we followed from data acquirement to the methodology that gave us the results in the next section.

2.4.1. Data Preparation

We started by acquiring the data from the NASA's HEASARC Data Archive[2]. Inside the data folders are, among others, all necessary event files (.evt), which hold the information of the photons that the detectors have received, images of the object area from both detectors, and orbit files, that have the data of the orbital location of the telescope.

Before starting any analysis, the data need to be cleaned and calibrated, so we begin by performing the 3 main processing stages of NuSTAR data analysis, using the "Heasoft version 6.22.1"[3]. These 3 processes are:

1. *Data Calibration:* Inputs the raw telemetry packets (*Level 0* science data), formats them in *.fits* format (*Level 1*) and produces calibrated event files (*Level 1a*).

2. *Data Screening:* Inputs the *Level 1a* data and filters it by applying cleaning criteria on specified orbital/instrument parameters and event properties, with the final product being calibrated and cleaned event files (*Level 2*).

3. *Products Extraction:* Inputs *Level 2* data and produces high-level scientific products (*Level 3*), such as light-curves, energy spectra, sky images, Ancillary Response Files (*ARF*) and Redistribution Matrix Files (*RMF*).

ARF contain a table of area values for several different energy ranges and *RMF* contain the instrument's response as a function of energy and PI channel in matrix format. Both *ARF* and *RMF* can be used for spectral modeling. The first two aforementioned processes (*Stage 1* and *Stage 2*) are called by a command of Heasoft, "*nupipeline*", that has a parameter that stops the procedure on the stage of the corresponding number's input. The third process (*Stage 3*) is called by the command "*nuproducts*".

At first, we run *nupipeline* for both NuSTAR detectors (FPMA and FPMB) and we stop it on Stage 2. We select an observation and a detector and we open the image of the object using *ds9*, by *IRAF*. Then, we create and save a circular region which corresponds to the majority of the incoming light and a similar region that corresponds to the background noise. These two *.reg* ASCII files will be used as inputs to the *nuproducts* command for data extraction. An example is shown in Figure 13.

2 https://heasarc.gsfc.nasa.gov/docs/archive.html
3 https://heasarc.gsfc.nasa.gov/docs/software/heasoft/

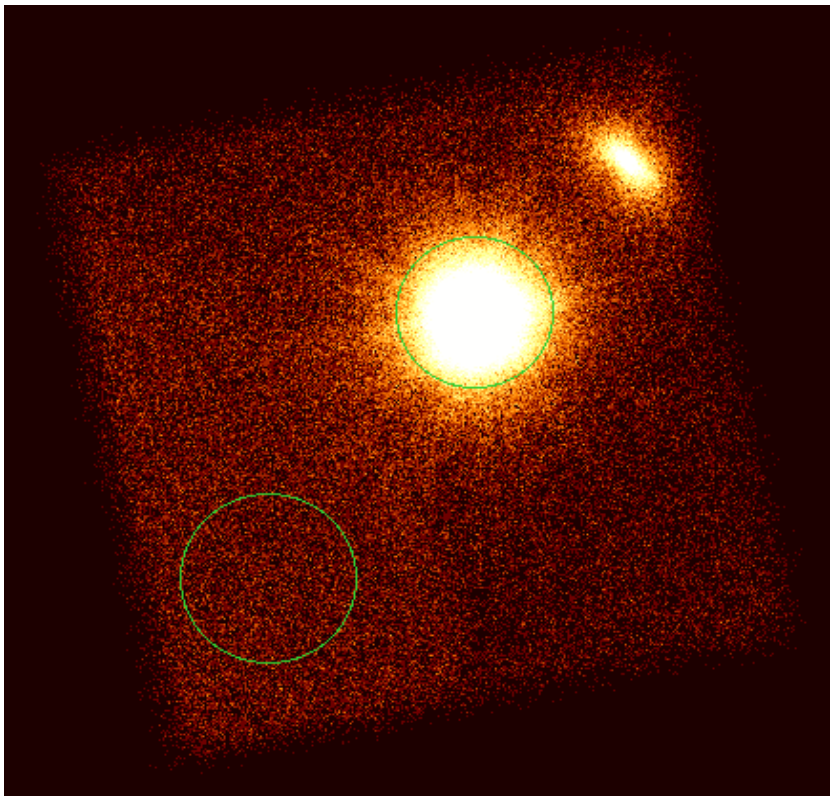

Figure 13: Selection of region files for the source and the background of our study (Swift J005139.2-721704)

Here we can see the image of the object and its surrounding area, as captured by FPMA on Obs1. The 2 green circles represent the regions mentioned above. Note that the object appearing on the top right is [MA93] 413 (or SXP 91.1), which is another HMXB (Monageng et al. 2019). The object was recognized using the SIMBAD Astronomical Database[4] in XMM data. We would also like to note that in the image, a cross can be discerned perpendicular to the rectangular shape of the image. This shape is caused by the detectors shown on Figure 8. The data are corrected in Stage 2 by dividing the counts image by the exposure map of NuSTAR. Finally, we repeat the aforementioned process for all observations and for both detectors.

On the last stage of the preparation, Stage 3, we used the following parameters to the *nuproducts* command:

- The "*barycorr*" was set to "*true*", so that the barycenter correction of the data is applied, for creating a common reference frame for time. This process requires as input the orbit file associated with the specific observation, mentioned at the beginning of this section.

- The "*binsize*" was set to "*1*" for a better resolution of energy spectra. This means that the data composing 1 bin have been accumulated over the duration of 1 second.

4 http://simbad.u-strasbg.fr/simbad/

As a last step, we ran the FTOOLS command "*grppha*" on the spectrum file. This command groups the energy spectrum in a way that ensures each bin to have a minimum of 20 counts in order to use chi squared statistics in the fitting. The new .pha file is then saved and ready for use. After the completion of these 3 stages the data are ready to be analyzed.

2.4.2. Modeling

In order to understand the structure and the undergoing motion of the accretion column, we take the energy spectrum and create a model from specific parts that each describe a different process. The model part selection is based on the shape of the spectrum and the possible features it contains (absorption or emission lines, for example). This whole procedure is carried out by XSPEC, an X-ray Spectral Fitting Package contained in FTOOLS. We also use XSPEC to fit the model to the data so it can give us the information needed to describe the energy spectrum. The models used in this study are listed in the following section.

The modeling procedure starts by loading the spectra for both FPMA and FPMB of a specific observation (.pha files) onto the XSPEC tool. The ARF, RMF and Background files are also required as input for both detectors. After that, we ignored the data that fell off the ***4 – 50 keV*** range. The reason is that below 4 keV, the NuSTAR instrument is not very reliable, and above 50 keV we noticed that the noise was at the same level as our data, something that affects the modeling process, essentially rendering it useless, since we cannot distinguish real data on a noise dominated area. This is showcased in the Figure 14.

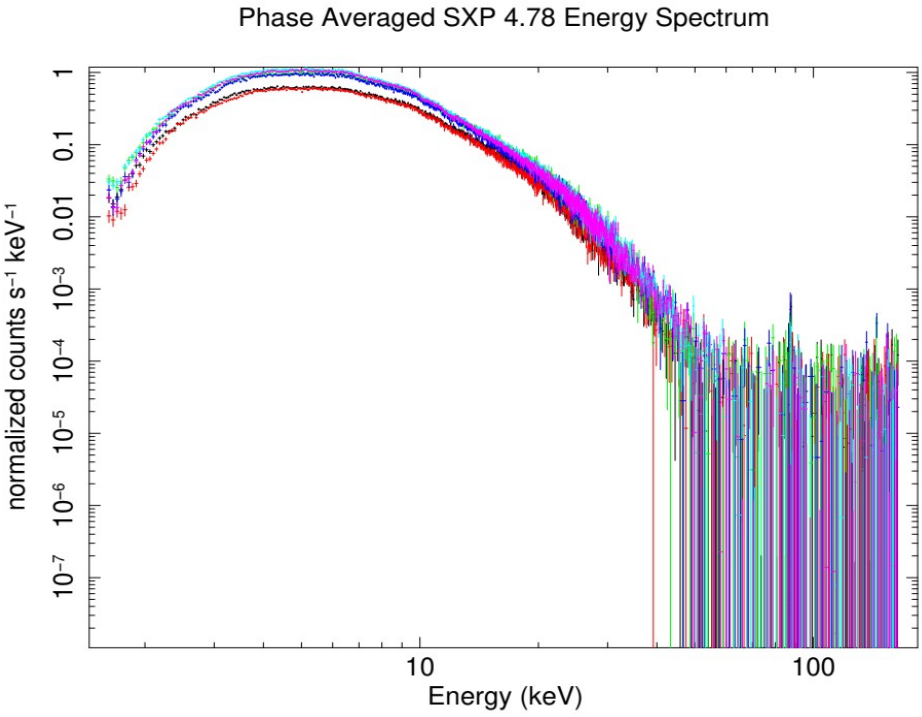

Figure 14: "Normalized Counts – Energy" diagram of the complete dataset of all 3 observations. Each observation consists of data from both FPMA and FPMB. Black and Red for Obs1, Green and Blue for Obs2 and Cyan and Pink for Obs3. We can clearly see the noise above ~50 keV which was ignored as mentioned before.

Every model we created always had the constant component, "***const***", and the component that takes into account the X-ray absorption due to the Interstellar Medium (ISM), calculated as an equivalent hydrogen column between us and the object, "***tbabs***". The *const* parameter of FPMA was set and frozen to the value of "*1*", so that a reference point can be created for the *const* parameter of FPMB. In addition, the $\mathbf{n_H}$ parameter of *tbabs* was set and frozen at $0.56 \times 10^{22}\ cm^{-2}$, as dictated by the best fit from Guillot et al., 2018. Starting off every model, we input the components and their mathematical relation. Then, we insert initial values and ranges that are commonly found in similar pulsars. Note that, besides *const*, every other FPMB parameter is set as equal to their FPMA counterpart. The addition of const to FPMB accounts for differences in the cross calibration of the 2 detectors. After running a number of fits, correcting values that were unreasonable and then rerunning them, we obtain a first picture of the parameter values. The next step was to run the "*error*" and "stap" command to improve the fit and calculate the errors.

The *error* command calculates the error bars of any parameter by first searching the lowest $\Delta\chi$ in a range around hard limits for a selected value. This is achieved by fitting every other model parameter for each iteration of the selected one. The range (meaning the maximum allowed value of $\Delta\chi$ on a hard limit) was set to the default $\Delta\chi = 2.706$, which corresponds to a 90% confidence region. When the algorithm finds the equivalent range in the parameter space it presets us with the error bars of that parameter. This process in further refined by the *step* command, which allows us to select a region in the parameter space and calculate the $\Delta\chi$ in a series of steps. We input a low limit, a high limit and the number of steps in which the algorithm will calculate the $\Delta\chi$ and we graph the results on a [$\Delta\chi$ – *value*] diagram. Then, we select the two values that have a $\Delta\chi$ of 2.706, which define the confidence range, creating the final error bars of the parameter. This extra procedure is necessary, especially in models comprised of many parameters. These models are unstable due to the large number of local minima in which the resulting confidence range of the *error* command might be stuck on. After completing these processes we can acquire the results of the modeling parameters. Note that all the commands that were used in the modeling procedure can be found in the NuSTAR Data Analysis Software Guide.

2.4.3. Models Used

The models we used were, in their majority, part of the XSPEC model library.

At the start of our analysis, we used the following model ***[1]*** :

[1] const · tbabs · powerlaw · fdcut

This model is a common start for accreting pulsars, since, at a basic level, the spectrum can be interpreted as a power law with a cutoff on larger energies.

The ***powerlaw*** component is described by the following formula:

$$A(E) = K_p E^{-\Gamma}$$

The parameters are listed below.

- ***Γ***: The dimensionless photon index of the power law
- K_p : The normalization factor in photons/keV/cm^2/s at 1 keV

The ***fdcut*** component (Fermi-Dirac Cutoff) was added and defined as follows:

$$\frac{1}{1+e^{\frac{E-E_{cut}}{E_{fold}}}}$$

The parameters are the following:

- E_{cut} : The energy where the spectrum begins its cutoff (in keV)
- E_{fold} : The energy where the spectrum folds (in keV)

After noticing a prominent line-like feature in the residuals around 6.5 keV (see Figure 18 in the next chapter), we added a Gaussian component to fit what was expected as an Iron emission line. The initial model was changed to the following model ***[2]*** :

[2] const · tbabs · (powerlaw · fdcut + gauss)

The ***gauss*** component is described by the following function:

$$A(E)=K_g\frac{1}{\sigma\sqrt{2\pi}}\exp[\frac{-(E-E_l)^2}{2\sigma^2}]$$

The parameters are as follow:

- E_l : The energy of the line in keV
- σ : The line width in keV
- K_g : A normalization factor in total photons / cm^{-2} / s, belonging to the line itself

The values of the parameters after the modeling process are presented in the next section.

Continuing the search for better models we tried the following:

[3] const · tbabs · compmag

The ***compmag*** model, discussed in the Section 1.4.2, is more detailed and can provide us with much more information about the geometry of the accretion column than a simple powerlaw (Farinelli, Ceccobello, Romano and Titarchuk, 2012). Since we are interested in that geometry, we selected compmag for the continuation of our analysis.

The parameters of the model are:

- $\boldsymbol{kT_{bb}}$: Indicates the temperature of the blackbody part of the spectrum
- $\boldsymbol{kT_e}$: This is the temperature of the electrons of the accretion column
- $\boldsymbol{\tau}$: The vertical optical depth of the accretion column, with the electron cross-section equal to 10^{-3} of the Thomson cross-section
- $\boldsymbol{\eta}$: The index of the velocity profile (valid if *betaflag* = 1)
- $\boldsymbol{\beta_0}$: Terminal velocity of the accreting matter at the neutron star surface in units of the speed of light "c" (valid if *betaflag* = 1)
- $\boldsymbol{r_0}$: The accretion column radius in Schwarzschild radii
- $\boldsymbol{A}$: The albedo at the neutron star surface (frozen at 10^{-3})
- A flag parameter "*betaflag*" (values: "*1*", or "*2*") that sets the velocity profile of the accretion column to:

$$\beta(z) = A\left(\frac{Z_S}{Z}\right)^{-\eta} \quad \text{where,} \quad A = \beta_0\left(\frac{Z_0}{Z_S}\right)^{\beta} \quad \text{, if } betaflag = 1$$

or

$$\beta(z) = -\alpha\,\tau \quad \text{, if } betaflag = 2$$

  Note that in this study we used *betaflag* = 1, due to its better results on the fit.

- A normalization factor

The reason that we ignored the Gaussian component for now is that the less parameters a model have, the more stable results it produces. By running the model ***[3]***, we obtain an initial image of how it behaves at the majority of the energy spectrum. Then, we just add the *gauss* component to our model and we input the values we have from the previous fit to the parameters of the *compmag* component. This make the fitting processes run faster and the subsequent results more reliable. The resulting model was the following:

[4] const · tbabs · (compmag + gauss)

It is important to note that, on some observations, after fitting the data with the model ***[4]***, we noticed a subtle feature in the residuals of the fit at the mid to low energies, an absorption line-like feature around 10-20 keV. This lead us to suspect that there is a cyclotron absorption line (CRSF) hidden in the spectrum, so we also added the *gabs* component to the fit, creating the model ***[5]***.

[5] const · tbabs · (gabs · compmag + gauss)

The reason behind the format of the model is that the ISM absorption acts on every component, since it is an observational matter and has nothing to do with the physics of the object. Also, the cyclotron line, fitted by a multiplicative component, will be multiplied with compmag, contrary to the gaussian one that is an additive model and is added to the product of the other two.

The *gabs* model is given by the following formula:

$$M(E)=\exp\left[-\left(\frac{par3}{\sqrt{2\pi}\,par2}\right)\exp\left(-\frac{1}{2}\left(\frac{E-par1}{par2}\right)^{2}\right)\right]$$

The parameters are:

- par1: The line energy in keV
- par2: The width of the line in keV
- par3: The line's depth, where the optical depth at the center of the line is: $par3/par2/\sqrt{2\pi}$

The models ***[4]*** and ***[5]*** are considered the best option and they were used for the whole Phase Resolved Analysis. The results of the modeling procedure are presented in the following section.

2.5. Phase Resolved Analysis

In the final step of our analysis, we split the data of each observation to 10 parts, with each part corresponding to a different spinning phase of the pulsar. This procedure was necessary to uncover changes in parameters during a complete rotation. Depending on the orientation of the accretion column relative to the observer, different heights contribute different amounts of photons, so for example, when a column is pointed directly into an observer, it is expected to have a spectrum with photons originated mostly from its upper section. Half of a semirotation later, when both beams (North and South) are pointed away from the observer, photons originated from the lower sections of the accretion column have a greater contribution in the spectrum, so any event happening in that vicinity can show up in the data.

2.5.1. Spin Period Search

The splitting was done using the XRONOS tools, a sub-package of FTOOLS. The commands we needed were the following:

- powspec: It creates a plot of the frequency spectrum of the pulses.

- efsearch: It searches for periodicities in the frequency spectrum by folding the data over a range of periods, starting from a custom initial value, and by finding the minimum of the chi-square (as a function of the periods).

Starting the analysis, we used the “powspec” command that gave us an initial value for the period search of 4.78 (s), which is consistent with the 2002 paper of S. Laycock et al. Next, we inserted the value of 4.78 (s) as an initial guess to the “efsearch” command and the algorithm continued the search for the value of the period that best folded the data. In the figures below we can see the results of this process.

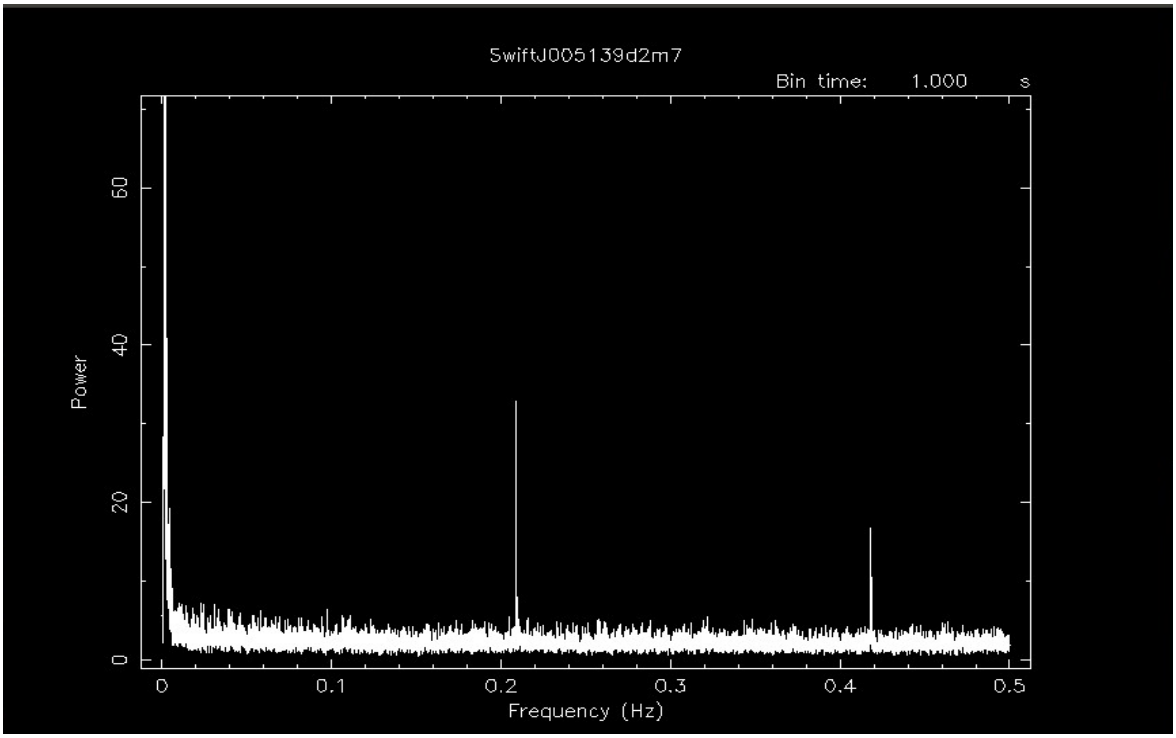

Figure 15: The output of "powspec" command as it searched for possible spin periods.

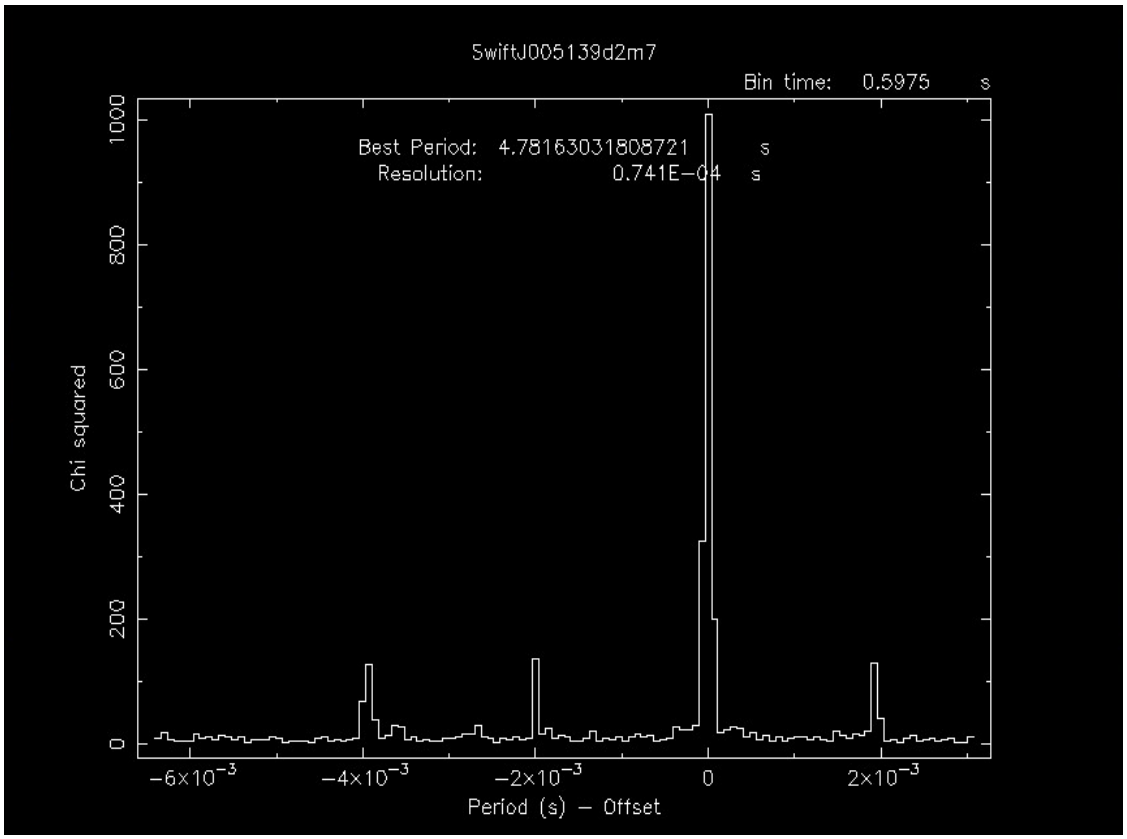

Figure 16: The results from the aforementioned run of efsearch for Obs1. We can see the Chi-Squared in an inverted diagram with the larger peak corresponding to the Best Period value. By inverting the diagram and measuring the Offset at the positive and negative value of Chi-Squared = 2.706 we can calculate the error bars of the spin periods (see Table 2.2).

After running this procedure for all 3 observations, we present the results in ***Table 2.2***.

Table 2.2
Spin Period results for the 3 observations

OBSERVATION ID	***Period (seconds)***	
	FPMA	***FPMB***
30361003002	$4.7816^{+0.0002}_{-0.0002}$	$4.7816^{+0.0002}_{-0.0002}$
30361003004	$4.7816^{+0.0002}_{-0.0002}$	$4.7816^{+0.0002}_{-0.0002}$
30361003006	$4.7816^{+0.0002}_{-0.0001}$	$4.7816^{+0.0002}_{-0.0001}$

2.5.2. Phase Binning

For the 10 part splitting we need to create a *GTI* (Good Time Intervals) file for each phase that we want. These files are used as a filtering method that select specific events to be used for the creation of the final products. In order to create a *GTI* file we started by using the command "*ftcalc*", which takes the data from the input Event File and creates a "*housekeeping*", or "*hk*" file, similar in nature. The new *hk* file has an extra column ("*PHASE*") we inserted, that was created by the calculation below:

$$\frac{(T - T_{init})\%\, P}{P}$$

where: ***P*** is the pulse period,
T is the time of the event,
$\boldsymbol{T_{init}}$ is the selected starting time
% is the ***mod*** function

This calculation gives us the phase of the pulsar with the starting value of 0 at the $\boldsymbol{Time_{init}}$. Now, we can use the "*maketime*" command of FTOOLS to create the *GTI* files we need by putting boundaries on the *PHASE* column. So, the first *GTI* will filter out events with *PHASE* values outside the 0 – 0.1 range, the second outside the 0.1 – 0.2 range, etc. Finally, we used the command "nuproducts" with the *GTI* file as an input and acquired the new spectra, one for each pulse phase.

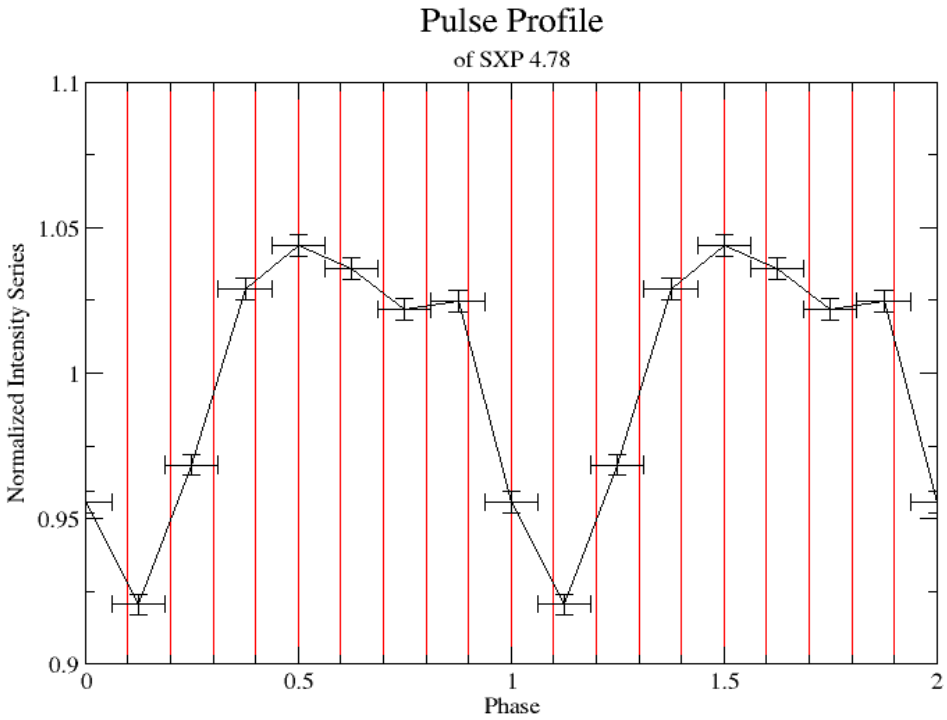

Figure 17: Pulse profile diagram for SXP 4.78 from Obs1 (FPMA) for 2 periods. This diagram showcases the split of our data into 10 parts (red lines). We have similar diagrams for both Obs2 and Obs3, as well as FPMB.

Chapter 3

Results

3.1. Phase Averaged Analysis Results

In this section we will present the results from the analysis of the total (phase averaged) spectra for the three observations we analyzed. For clarification purposes, the *Ratio* is defined as the data divided by the model and the *Residuals* are defined as the data minus the model.

3.1.1. Initial Models

We begin by presenting the results of the power-law with a Fermi-Dirac cutoff model (Model ***[1]***). As we can see from Figure 18, these models gave unacceptable fits to the data from all three observations.

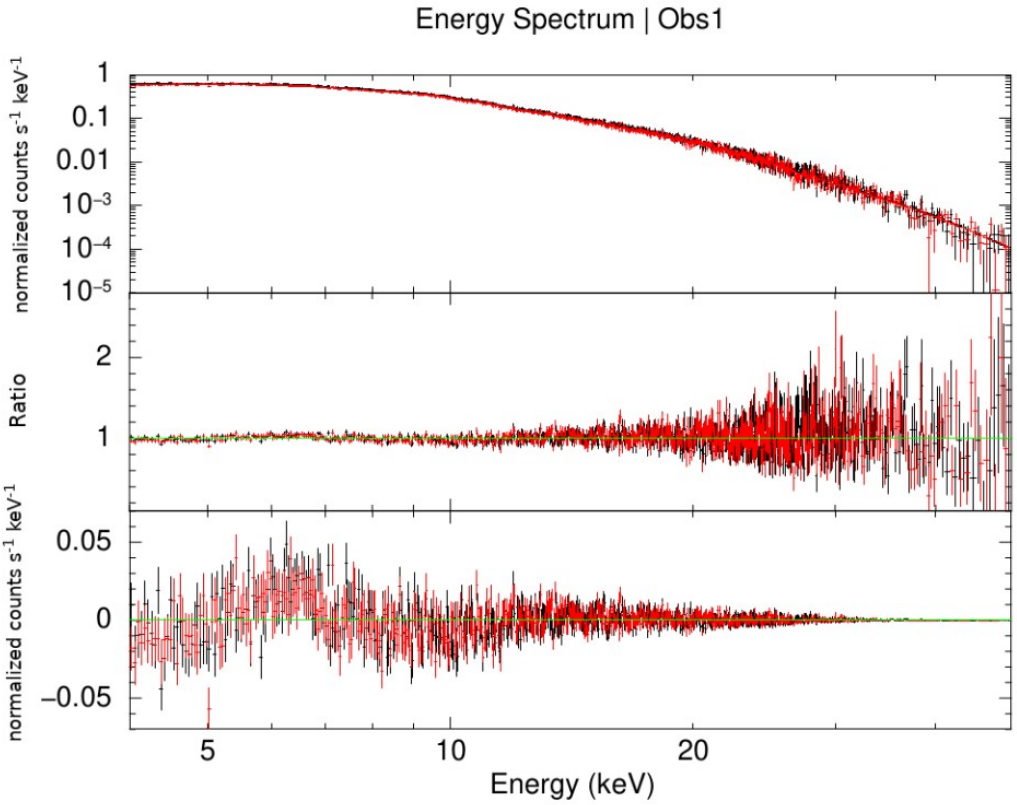

Figure 18: (from top to bottom) Energy Spectrum for Obs1 with the fitted Model [1], the model ratio and its residuals. Next follow the same diagrams for Obs2 and Obs3.

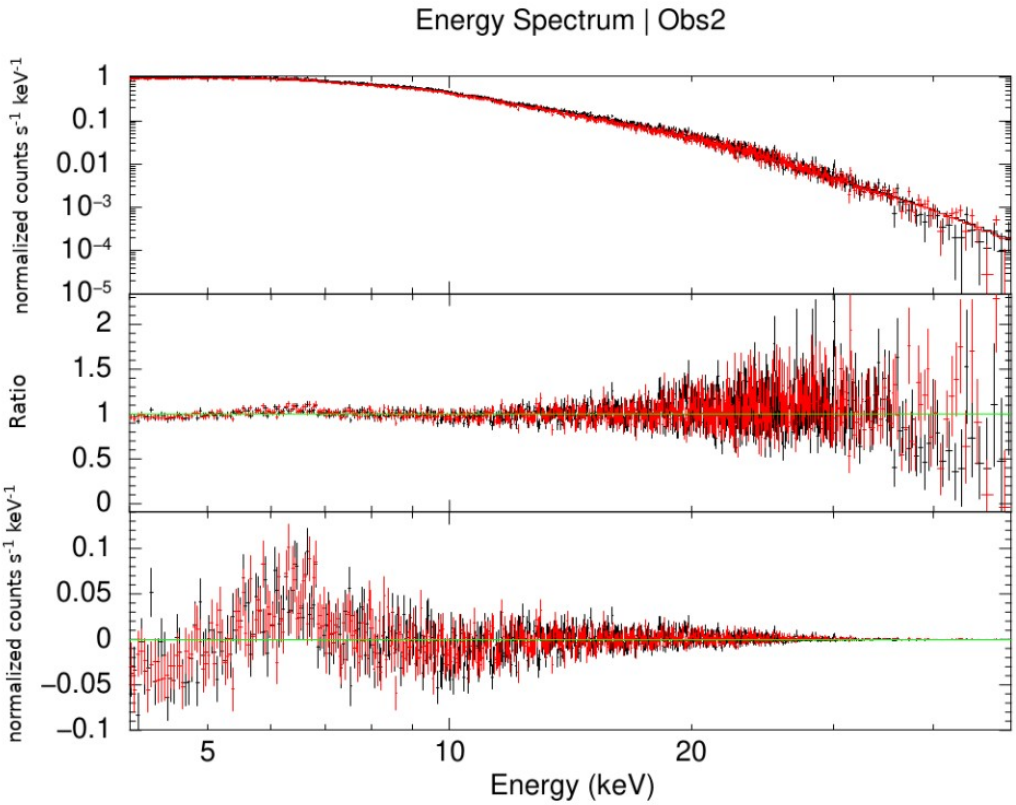

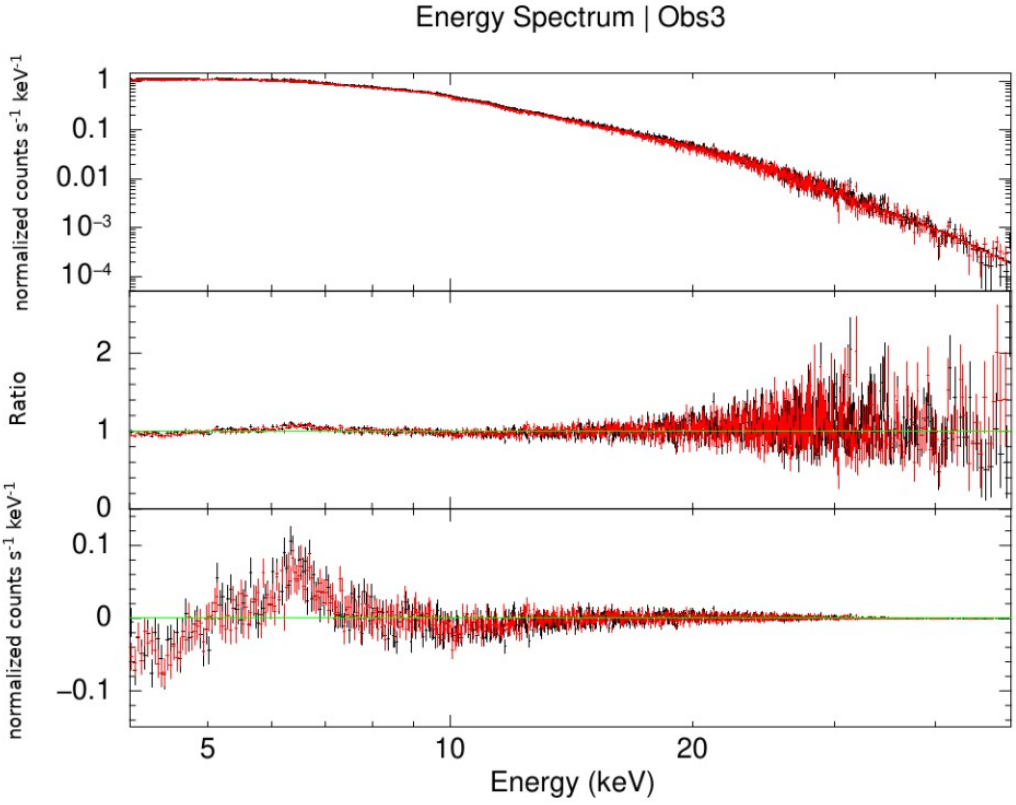

The aforementioned diagrams for Obs2 and Obs3.

We can clearly distinguish a line-like feature on the range of *5 - 8* keV that has high residuals, so we concluded that we need to add the Gaussian component, possibly corresponding to an Iron emission line that might be expected, as discussed in the previous section. We also observe that in each observation, the feature becomes more prominent (see residuals on Figure 18. As mentioned before, SXP 4.78 increased its luminosity as the days progressed (see Figure 11), therefore we can conclude that the line-like feature becomes stronger in higher luminosities.

We then fitted a model including a cutoff power-law and a Gaussian line (Model ***[2]***). This model gave very good results as is seen in ***Table 3.1*** and Figure 19.

Table 3.1
Spectral fits of Model [2] for the 3 observations

OBSERVATION ID	**30361003002**	**30361003004**	**30361003006**
Flux (x10^{-10} ergs/cm^2/s)	2.5746	3.7967	4.3336
$Const._{FPMB}$	$1.020^{+0.004}_{-0.004}$	$1.023^{+0.005}_{-0.005}$	$1.022^{+0.003}_{-0.003}$
N_H (10^{21} cm^{-2})	0.56 (fixed)	0.56 (fixed)	0.56 (fixed)
Γ	$1.22^{+0.04}_{-0.03}$	$1.26^{+0.06}_{-0.07}$	$1.22^{+0.05}_{-0.06}$
Kp (photons / cm^{-2} / s)	$267^{+9}_{-1} x 10^{-4}$	$49^{+5}_{-5} x 10^{-3}$	$65^{+8}_{-8} x 10^{-3}$
Ecut (keV)	11.7^{+1}_{-1}	9.2^{+2}_{-3}	5.2^{+3}_{-3}
Efold (keV)	$8.1^{+0.2}_{-0.2}$	$8.8^{+0.3}_{-0.3}$	$9.3^{+0.2}_{-0.3}$
E_line (keV)	$6.2^{+0.2}_{-0.3}$	$6.0^{+0.3}_{-0.6}$	$5.8^{+0.3}_{-0.5}$
σ (keV)	$1.0^{+0.3}_{-0.2}$	$1.4^{+0.4}_{-0.3}$	$1.6^{+0.4}_{-0.3}$
*KG (*photons/keV/cm^2/s*)*	$2.9^{+1.0}_{-0.7} x 10^{-4}$	$11^{+8}_{-4} x 10^{-4}$	$1.6^{+1.0}_{-0.5} x 10^{-3}$
χ^2 / *dof*	1.03/1365	1.014/1286	1.044/1461

The flux of each observation was calculated by running the “flux” command of XSPEC which integrates the spectral model within an energy range. In our analysis all fluxes are reported in the 4-50 keV band and they are not corrected for absorption. The energy of the Gaussian line is consistent within the errors with an Fe line at 6.4 keV. What is interesting is that the line has considerable width (σ~1keV). We clearly see that there is a positive correlation between the line flux and the total flux of the spectrum, suggesting that the intensity of the line increases as the source becomes brighter. The last row shows the reduced chi-square (χ^2) and the degrees of freedom (dof) of each model. These values (close to 1) are considered to be a good indication that the fit is good. Figure 19 shows the best-fit model, the residuals and ratio for each of the three observations.

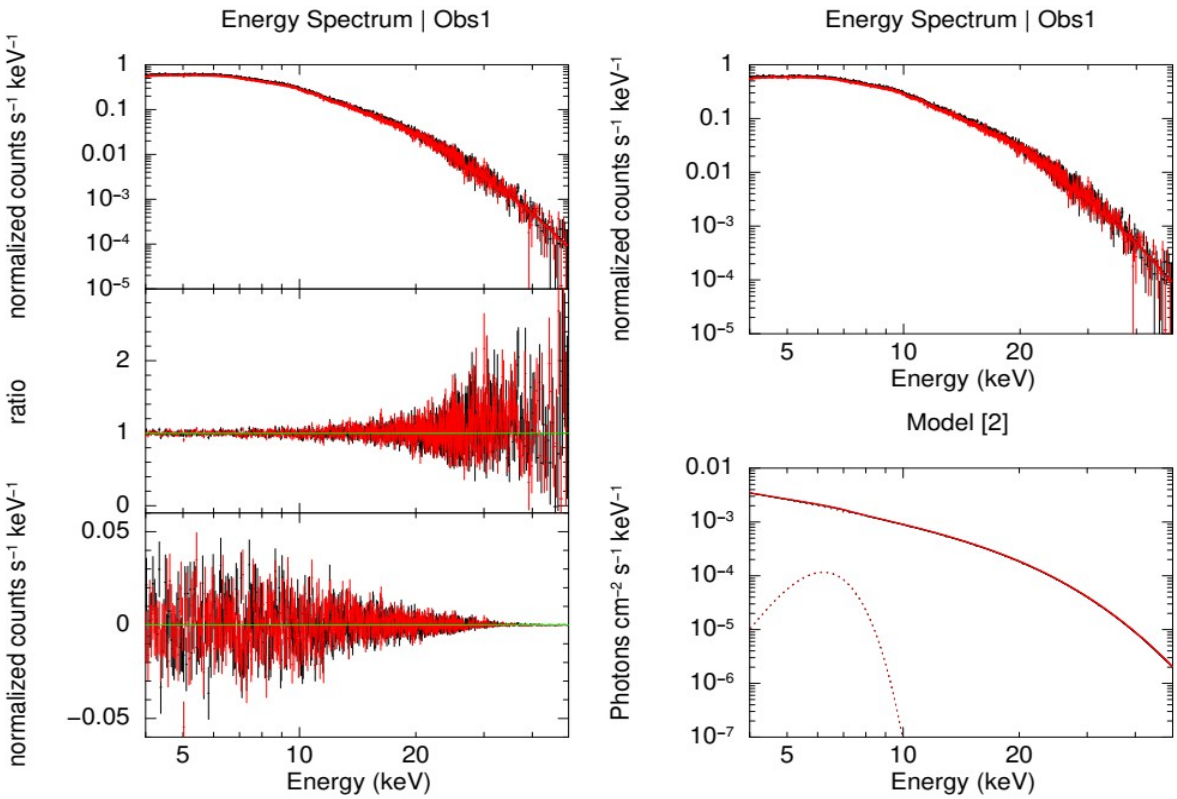

*Figure 19: Energy Spectra of the 3 observations fitted with Model **[2]** (see next page too). Each left figure consists of, from top to bottom, the energy spectrum of Obs1 (on this page) and Obs2 and Obs3 respectively (in the next page), the ratio and the residuals with respect to the model. On the right side, we can see the energy spectrum again, for convenience, and below, the best-fit model. We can see the main power-law continuum with the cut-off (solid line) and the addition of the Gaussian component (dotted line).*

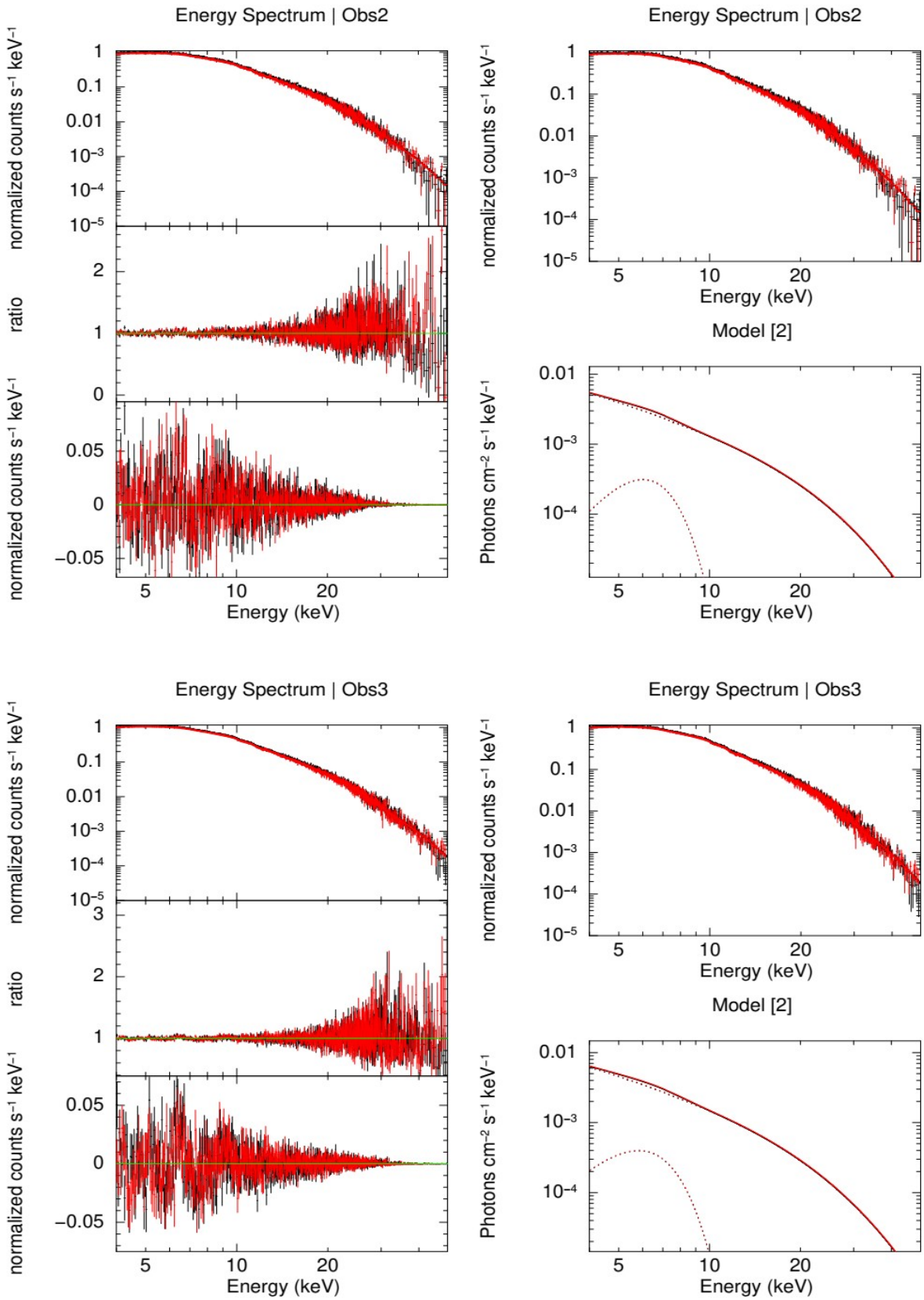

The aforementioned diagrams for Obs2 and Obs3.

Judging by the low residuals in all 3 spectral fits and the excellent reduced χ^2 (there is a feature at 6.4 keV in Obs 3 indicating probably that the fitted line is broader than it should be), we can say that Model ***[2]*** is a good representation of the energy spectrum of all 3 observations.

Although Model ***[2]*** is a good fit, it is a phenomenological model and it does not give us any information on the physical conditions in the accretion column. In order to obtain a deeper understanding of the structure of the accretion column, in the next sub-sections we discuss results from more physically motivated models: Model ***[4]***, using a combination of the compmag model and a Gaussian line referred to as compmag-gauss Modeling (*CG Modeling*) and for Model ***[5]***, which is the same as Model ***[4]*** with the addition of the *gabs* component for the cyclotron line (*CGG Modeling*). We would like to note that the Gaussian feature cannot perfectly fit the Iron emission line due to the fact that it appears to have an unusual (non-Gaussian) shape. This is more prominent in the residuals of the fit of Model ***[2]*** in Obs3 (see Figure 19) and will be discussed in *Section 4.1*.

3.1.2. CG Modeling

In ***Table 3.2*** we present the best-fit model parameters for each of 3 observations using Model ***[4]***. We note that these are the phase-averaged spectra, i.e. including contribution from all phases. This is mentioned to distinguish these results from the ones obtained during the Phase Resolved Analysis on *Section 3.2* during the fitting of the same Model ***[4]***.

Table 3.2

Spectral fits of Model [4] for the 3 observations

OBSERVATION ID	**30361003002**	**30361003004**	**30361003006**
Flux (10^{-10} ergs/cm^2/s)	2.5769	3.8028	4.3357
N_H (10^{21} cm^{-2})	0.56 (fixed)	0.56 (fixed)	0.56 (fixed)
kT_{bb}	$0.458^{+0.3}_{-0.5}$	$1.062^{+0.05}_{-0.04}$	$1.105^{+0.01}_{-0.002}$
kT_e	$2.932^{+0.6}_{-0.6}$	$4.028^{+0.09}_{-0.09}$	$3.938^{+0.06}_{-0.09}$
τ	$1.0677^{+0.03}_{-0.03}$	$0.763^{+0.006}_{-0.006}$	$0.679^{+0.008}_{-0.006}$
η	$0.833^{+inf}_{-0.2}$	$0.958^{+0.01}_{-0.01}$	$0.681^{+inf.}_{-0.2}$
β_0	$0.152^{+0.04}_{-0.04}$	$0.106^{+0.003}_{-0.003}$	$0.105^{+0.08}_{-0.1}$
r_0	$0.448^{+inf}_{-0.448}$	$0.553^{+inf.}_{-0.553}$	$0.545^{+inf.}_{-0.5}$
$norm_{compmag}$	655^{+inf}_{-500}	57^{+64}_{-9}	$53.4^{+0.4}_{-0.3}$
E_{Fe}	$5.933^{+0.2}_{-0.4}$	$6.44^{+0.09}_{-0.1}$	$6.527^{+0.05}_{-0.05}$
σ_{Fe}	$1.3^{+0.3}_{-0.2}$	$0.4^{+0.2}_{-0.1}$	$0.27^{+0.07}_{-0.06}$
$norm_{Fe}$	$6^{+3}_{-2} x 10^{-4}$	$6^{+3}_{-2} x 10^{-4}$	$1.54^{+0.3}_{-0.2} x 10^{-4}$
C_{FPMB}	$1.020^{+0.002}_{-0.004}$	$1.023^{+0.005}_{-0.004}$	$1.022^{+0.003}_{-0.003}$
χ^2_{reduced} / d.o.f	1.024/1362	1.003/1290	1.006/1464

We can see that the values of χ^2_{reduced} are excellent, as was Model ***[2]***. The Figure 20 below, and in the next page, showcases the graphical representation of the ***Table 3.2***.

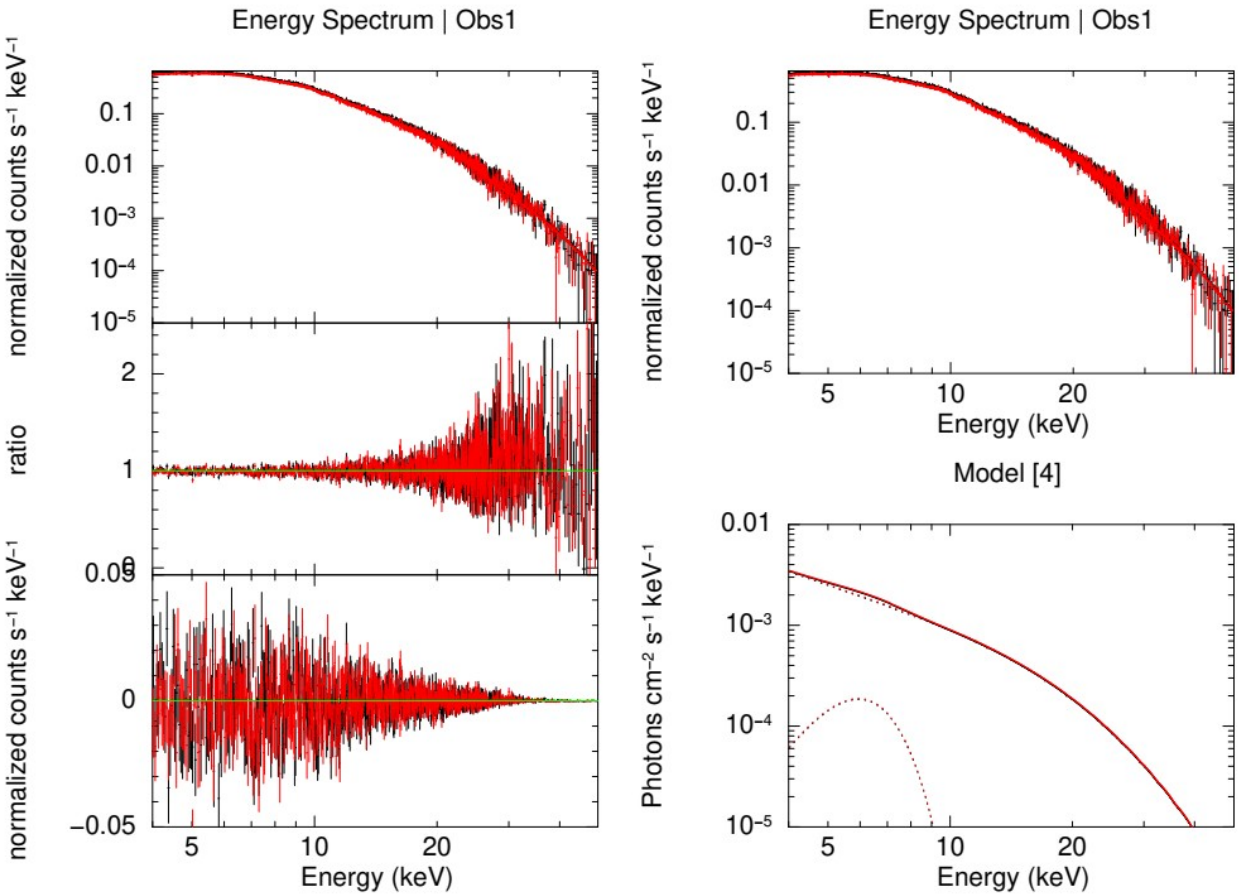

*Figure 20: Energy Spectra of the 3 observations fitted with Model **[4]** (see next page too). Each left figure consists of, from top to bottom, the energy spectrum of Obs1 (on this page) and Obs2 and Obs3 respectively (in the next page), the ratio and the residuals with respect to the model. On the right side, we can see the energy spectrum again, for convenience, and below, the best-fit model. We can see the main compmag power-law continuum and the addition of the Gaussian component (dotted line).*

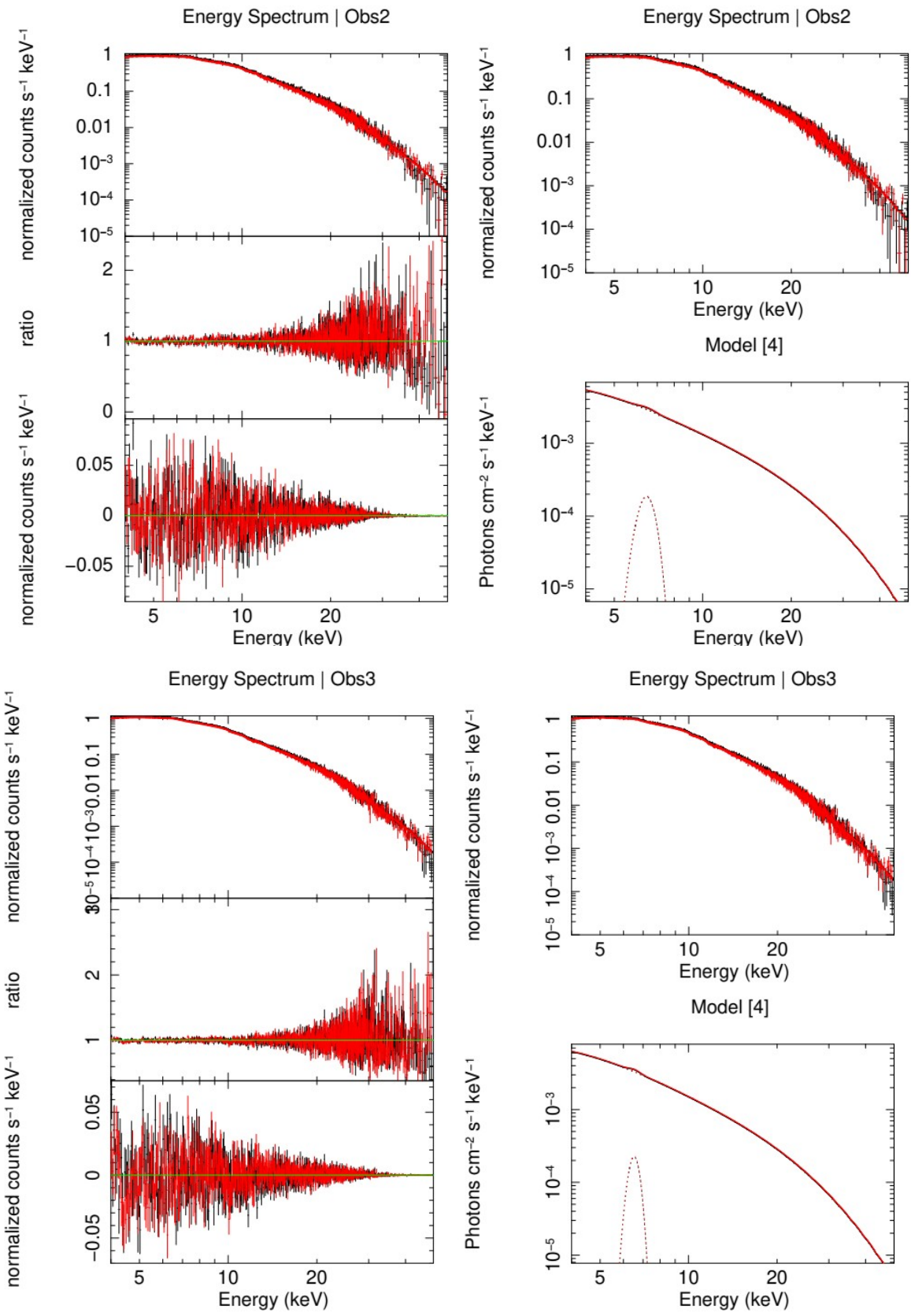

The aforementioned diagrams for Obs2 and Obs3.

3.1.3. CGG Modeling

Using the Model ***[5]*** and the best-fit model parameters obtained for Model ***[4]***, we searched for a possible Cyclotron Resonant Scattering Feature. By looking at the residuals and the ratios of the best-fit models to the phase-averaged spectra of all 3 observations, there is no indication for any additional spectral feature, but we decided to search for it nonetheless. As expected, the new fit barely changed the reduced chi-square at the 2^{nd} - 3^{rd} decimal place, a change easily justified by the addition of 3 more components in the model, therefore we can confidently reject it.

Although the Phase Averaged Spectra may not show signs of a cyclotron line, it is possible for a CRSF to be present in spectra extracted from individual phases. The CRSF is produced when continuum photons from the accretion columns undergo resonant scattering by electrons in different Landau levels. Since the magnetic field strength is a string function of distance from the pulsar poles and at different pulse phases we observe different regions of the accretion column one would expect to see variations in the strength and the energy of the CRSF depending on the pulse phase. This is the reason we proceeded to use Model ***[5]*** in our Phase Resolved Analysis, for the possibility of the absorption line to be found in a specific phase of a pulse.

3.2. Phase Resolved Analysis Results

In this section we will present the results from our Phase Resolved Analysis *(PRA)* in the form of Phase diagrams. We fit the spectra extracted for each pulse phase (as described in Section 2.5) with Model ***[4]*** combining the compmag model with a Gaussian emission line, a CRSF, and photoelectric absorption. We fit each of the 10 sub-phases for each observation with this model. First of all, Figure 21 shows the flux of the 3 observations, taken from the FPMA detector of each one using the “flux” command on the fitting of Model ***[4]***.

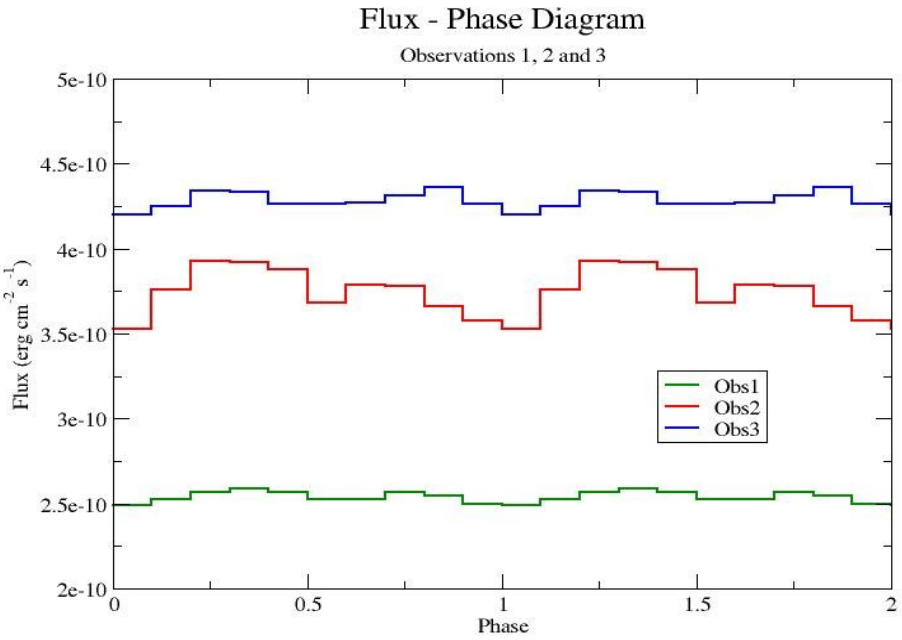

Figure 21: Flux as a function of phase taken from the best model fit of the FPMA data. Observations 1, 2 and 3 are colored green, red and blue respectively. The rotational cycle has been plotted twice for convenience purposes.

In Figure 21 we can see that Obs3 is approximately 1.7 times brighter than Obs1 and 1.2 times brighter than Obs2, while Obs2 is approximately 1.5 times brighter than Obs1. We can also observe that Obs2 appears to have a more variable flux than the other two.

3.2.1. Phase Resolved Parameters

After acquiring the first results, we noticed that many model parameters changed their values only inside of their error range relative to the phase. That was expected, as we noted in Section 1.4.2, due to their nature. Parameters like the blackbody component (***kT_{bb}***), the index of the velocity profile η and the radius of the accretion column r_0 are independent of the rotational phase and the fact that they remained constant is a reassurance that the modeling procedure performed adequately. All the parameters of the Gaussian component remained constant as well, as expected too.

The Blackbody Temperature was constant because of the region its photons originated. No matter the angle of observation of the accretion column, the same black-body seed photons interact with the accretion column electrons resulting in the observed spectrum. This is the reason the value of kT_{bb} remained constant within its error range. The radius of the accretion column (***r_0***) was one of the unconstrained parameters. In addition to that, we expect the accretion column to maintain its radius independent on the observation angle. The index of the velocity profile (***η***) was also unconstrained enough to presume it constant. Of course, the 3 Gaussian parameters remained constant as well, as they originate from the accretion disk, which does not change its angle as the pulsar rotates. As a result, we decided to freeze the parameters to their best-fit values of the phase-averaged fit (see ***Table 3.2***), to relieve pressure from the algorithm, since changing them does not serve any purpose.

The remaining 3 parameters were the parameters that appear to change with the phase of the rotation. These are the temperature of the electrons of the accretion column (***kTe***), the vertical optical depth of the accretion column (***τ***) and the terminal velocity of the accreting matter at the neutron star surface (***β_0***). Consequently, the Phase Resolved Analysis will present results from there 3 parameters (***kTe, τ*** and ***β_0***).

We expect that, when we observe the accretion column from the top (pointed at us with higher overall luminosity), we will receive photons that originated from lower-energy electrons on higher altitudes in the accretion column, where the density of the material is lower. We also expect to observe higher values for β_0 since the electrons have not yet slowed down from the accumulated matter at the bottom. In contrast, when we observe the accretion column from the sides (with lower overall luminosity), we expect to observe photons originating from electrons with higher temperature, as they lie in the lower parts of the column, near the surface of the pulsar. We also expect their speeds to be lower, due to the gas slowing down as it accumulates near the pole.

3.2.2. CG Modeling (PRA)

Obs1 (30361003002)

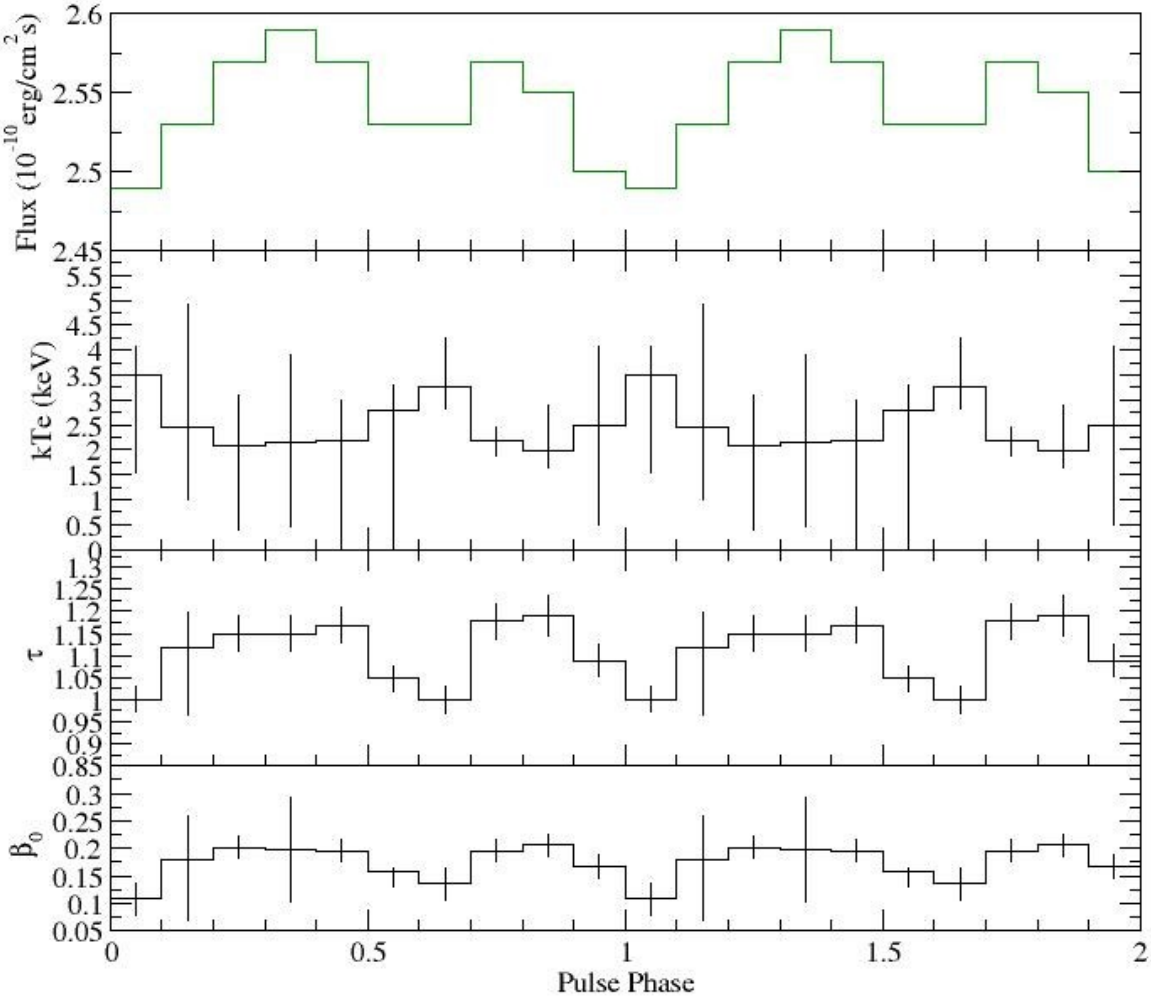

Figure 22: Spectral parameters as a function of Phase resulting from GC modeling (Model [4]) for Obs1. From top to bottom: Flux, Electron Temperature (kTe), Vertical Optical Depth (τ) and the Terminal Velocity of the Accreting Matter (β_0).

By looking at Figure 22 we can see a correlation between the 3 parameters and the flux. As the flux increases, the electron temperature (*kTe*) seems to decrease and vise versa. Due to the large error bars of *kTe* though, we should exercise caution in reaching that conclusion. We can also observe that the vertical optical depth (τ) and the terminal velocity of the accreting matter (β_0) tend to follow the flux, with all 3 reaching their highest and lowest values at the same phase. The same behavior also appears on the next 2 diagrams for Obs2 and Obs3.

Obs2 (30361003004)

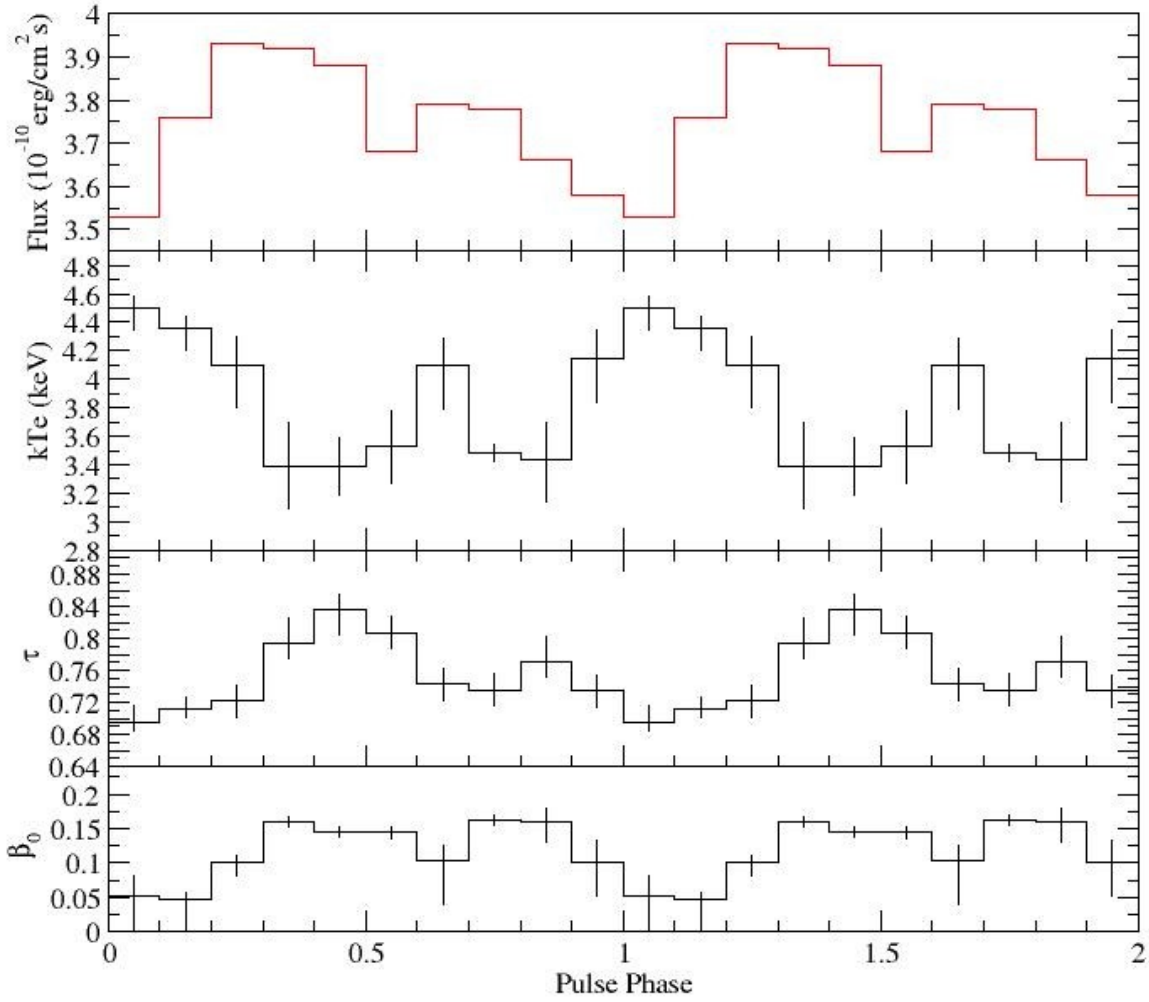

Figure 23: Spectral parameters as a function of Phase resulting from GC modeling (Model [4]) for Obs2. From top to bottom: Flux, Electron Temperature (kTe), Vertical Optical Depth (τ) and the Terminal Velocity of the Accreting Matter (β_0).

By comparing Figures 22 and 23, we can observe that the larger variability of the flux in Figure 23 corresponds to a larger variability on all other parameters, especially on the Electron Temperature. This is also true in the next diagram for Obs3.

Obs3 (30361003006)

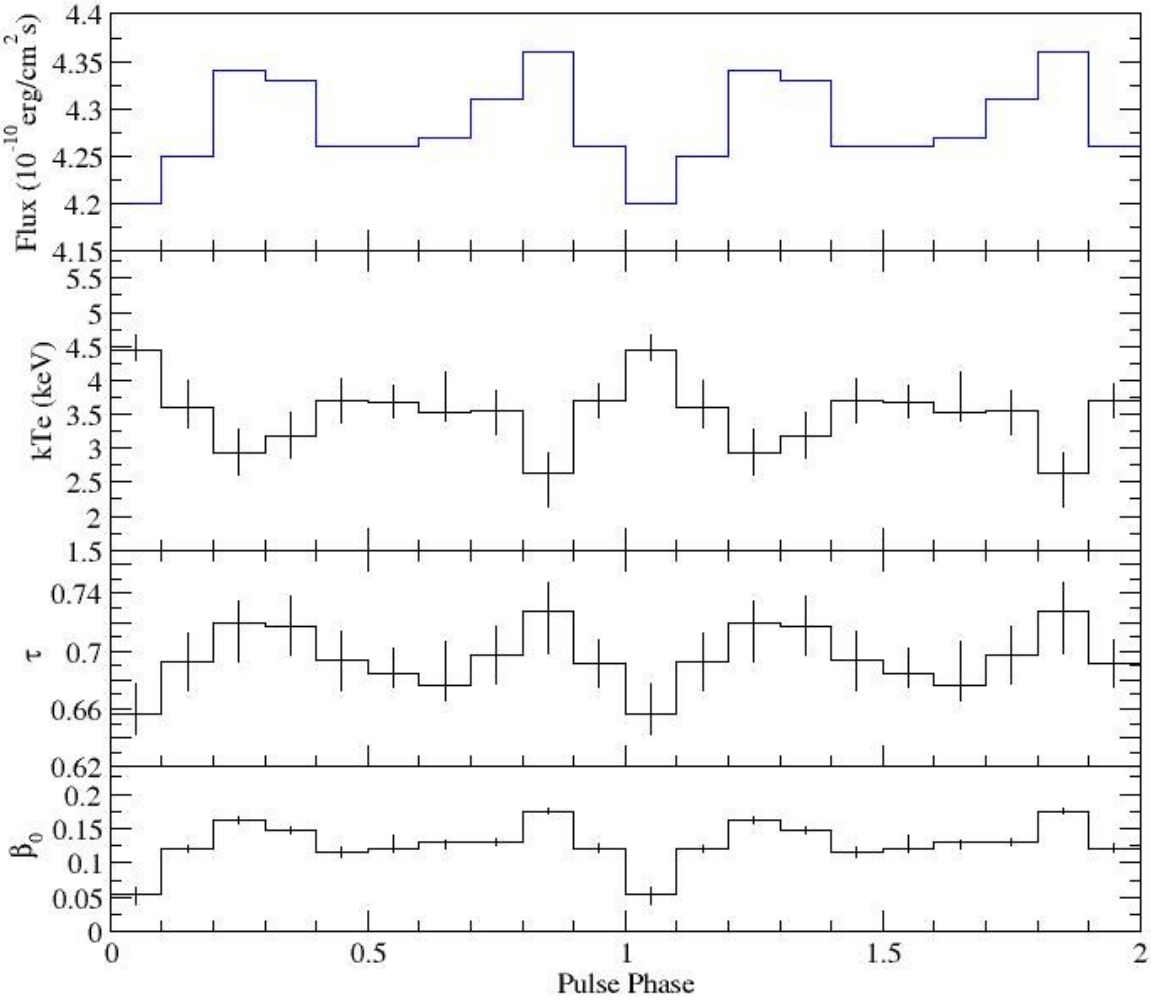

Figure 24: Spectral parameters as a function of Phase resulting from GC modeling (Model [4]) for Obs3. From top to bottom: Flux, Electron Temperature (kTe), Vertical Optical Depth (τ) and the Terminal Velocity of the Accreting Matter (β_0).

If we examine Figure 24, we can observe the small confidence ranges of the modeling parameters, due to the high amount of data received during Obs3, caused by the high flux of the source.

3.2.3. CGG Modeling (PRA)

As mentioned before, it is possible for a CRSF to be visible only in a specific phase of a pulse in a pulsar's spectrum, making it unnoticeable when observing a phase averaged pulse profile. This is the reason behind our decision to fit each phase of every observation using Model ***[5]***. By inserting the final values of Model ***[4]*** for every parameter of the *compmag* and *Gaussian* component as initial values for the same components Model ***[5]***, we began the search of the absorption line. Our initial guess was around 10-20 keV, but as the model failed to reveal a CRSF, we expanded the search to higher energies. All 10 phases did not show any absorption line-like feature, so we discarded Model ***[5]***.

Chapter 4

Discussion

The aim of this project was to perform spectral and timing analysis of Swift J005139.2-721704, an accreting X-ray pulsar, so we can study its accretion column by fitting the Becker-Wolff model (Becker and Wolff, 2007) for its spectrum. The timing analysis was based on the splitting pulse profile of the pulsar to 10 parts (10 phases), with each phase having data from a different angle of the accretion column. When the flux was high, we viewed the column directly and when the flux was low, the column was seen from the side. Although we can infer those general facts with certainty, any further propositions have to take into account that the pulsar is a point-like source and in each phase we are receiving photons from all parts of both the North and South accretion columns. This lack of an exact localization makes our problem significantly more complex and our deductions considerably less certain. The phase resolved spectroscopy allows us to break this degeneracy to some extent.

In this chapter we will discuss the 3 accretion column parameters that appeared to change during the pulsar's rotation. We will also examine the nature of the Iron emission line around 6 keV witnessed in every spectrum.

4.1. Accretion Column

The material inside the accretion column is optically thick, with its density increasing as the height from the pulsar's pole decreases. This fact is affecting the photons in different ways depending on their source and the path they take inside the column, so we can expect the spectrum to change with the viewing angle. In this section we will consider the low and high flux pulse phases.

Table 4.1
Low and High Flux Phases for the 3 observations

OBSERVATION ID	***Pulse Phases***	
	High Flux	***Low Flux***
30361003002	0.2 – 0.4 , 0.7 – 0.8	0.5 – 0.6 , 0.9 – 1
30361003004	0.2 – 0.4 , 0.6 – 0.7	0.5 , 0.9 – 1
30361003006	0.2 – 0.3 , 0.8	0.4 – 0.6 , 1

4.1.1. High Flux

When the flux reaches its highest values, we observe the accretion column closer to a pole-on view, with the main source of X-ray photons being the inside of the column itself. As mentioned in the previous chapter, the electron temperature reaches its lowest values when we look inside the column, whereas the vertical optical depth (τ) and the terminal velocity of the accreting gas (β_0) reach their maximum.

In order to understand those relations between the model parameters we need to consider the approximate region of the column this emission is coming from. We base our analysis in a schematic of the accretion flow such as the one presented in Figure 25, where the observed emission in the high-flux phases is has a larger contribution from the pencil beam. The values of τ (close to 1) show us that when viewing the accretion column from the top, we can see the upper parts of the inside of the structure, where matter has already free-falling towards the pole. That also explains why β_0 reaches its highest values during those phases, at around 0.15% to 0.175% the speed of light, although this is much lower than the maximum it is expected to reach (~70% the speed of light). Probably it means that the shock forms higher because of radiation pressure, so the gas does not attain its maximum velocity. This may also explain the relatively low vertical optical depth, since, if the flow stalls at a higher altitude, the density and the path within the column are expected to be lower. For the same reason the electron temperature is lower, since at a higher height the electrons do have as high temperature.

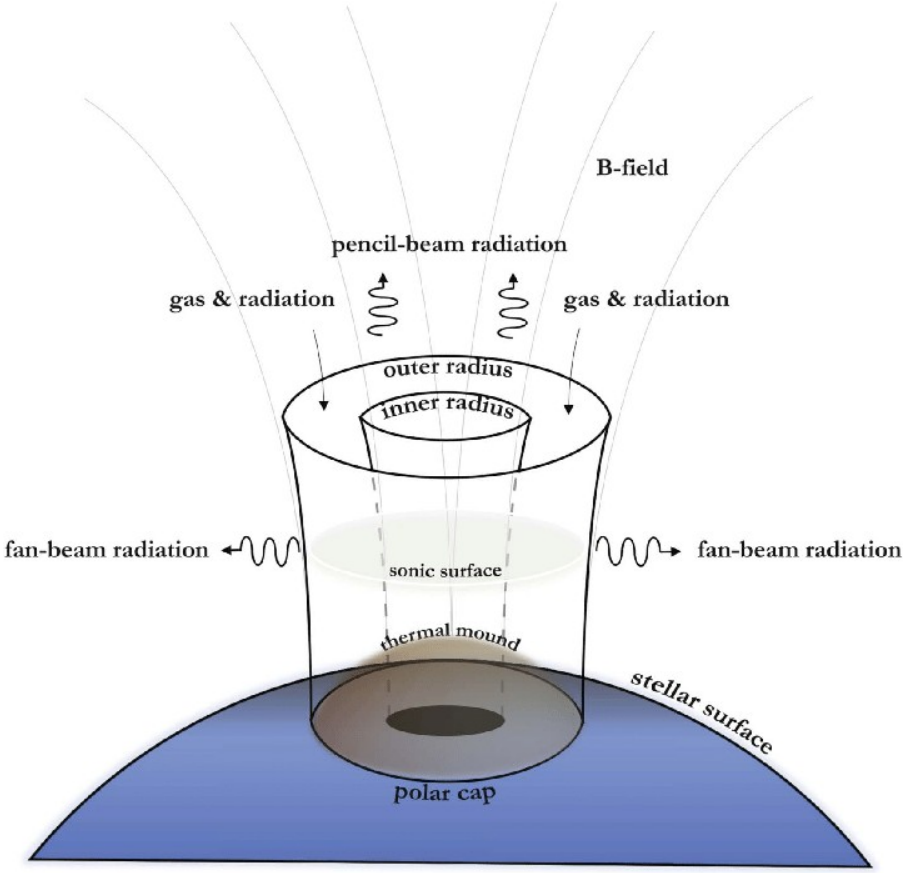

Figure 25: Accretion column photons and their origin. We can see that the viewing angle corresponding to the high flux is dominated by pencil-beam radiation and the side view (low flux) by fan-beam radiation. (West et al. 2016)

4.1.2. Low Flux

When we select a phase that has a low flux, both the accretion columns point away from our line of sight. In Figures 22-24 we can see the values of τ and β_0 are at their minimum at those phases, while kTe is at its maximum. The lower values of τ indicate that we can see deeper into the accretion column than when viewing from the top. The location the photons originated lays on top of the thermal mound, where the in-falling gas has slowed down and the photons created are diffusing through the column until they escape from the side. Figure 25 showcases this process as “fan-beam radiation”. These photons are more energetic than the ones received from the top view, with their kTe ranging from 3.5 keV to 4.5 keV. This is because these electrons are located closer to the pulsar surface and they have released a larger fraction of their dynamical energy. In addition, since these electrons are slowly sinking towards the surface of the neutron star, they are expected to have lower velocities than their maximum velocity at the sonic point (see Figure 25).

4.1.3. Parameter Time Evolution

In this section we will discuss the change of the 3 parameters (kTe, τ and β_0) as a function of time between the 3 observations. We selected the phases with the highest and lowest values of flux and we plotted the 3 parameters in 3 diagrams. Each diagram includes the values of the parameter when viewing the accretion column from the top (high flux) and from the side (low flux). By examining Figures 26-28 we can expect the values of the other phases of each parameter to fall between the red and black points of the diagrams, during one observation.

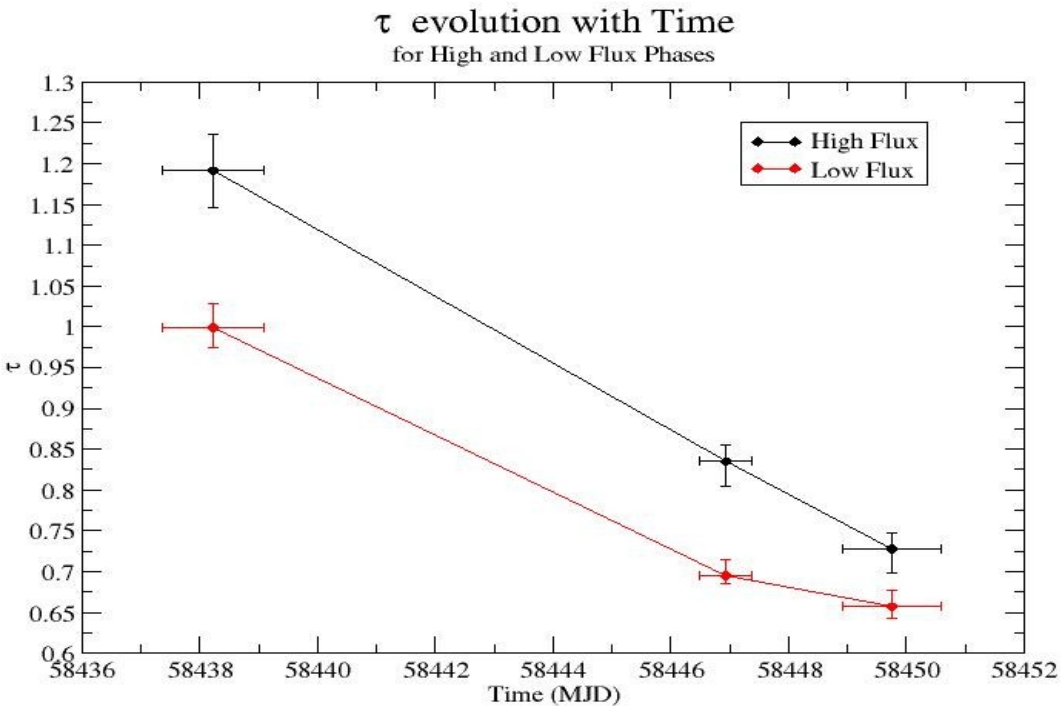

Figure 26: Vertical Optical Depth as a function of time, from Obs1 to Obs3 (the duration of each observation is represented by the error bars on the Time axis).

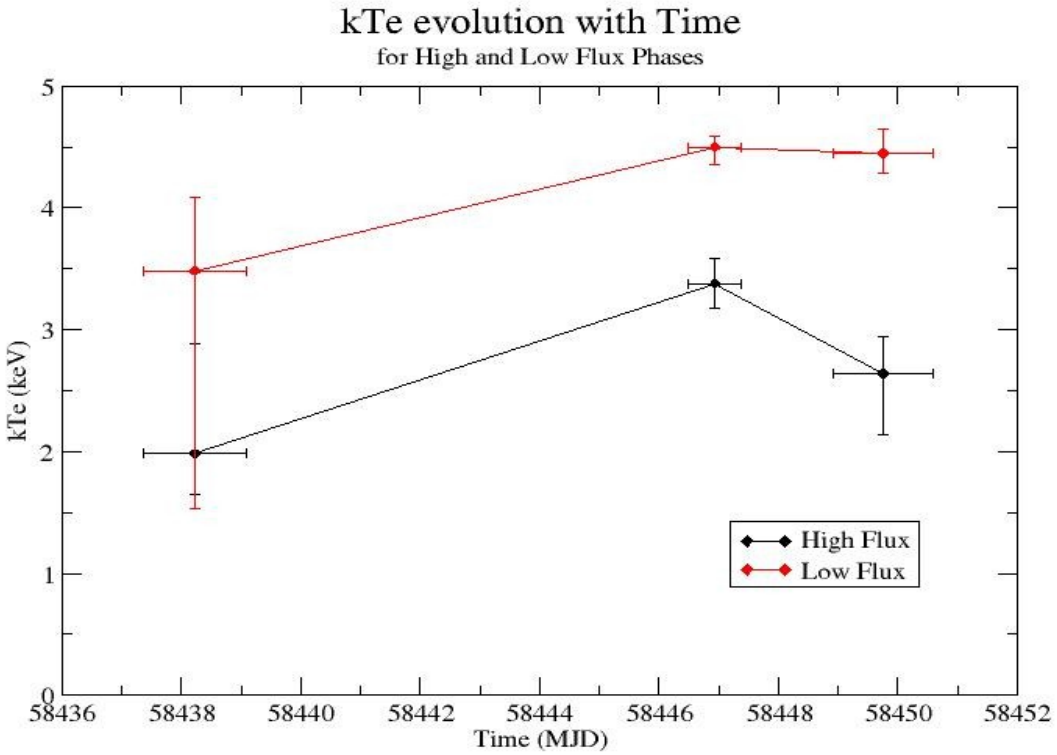

Figure 27: Electron Temperature as a function of time, from Obs1 to Obs3 (the duration of each observation is represented by the error bars on the Time axis).

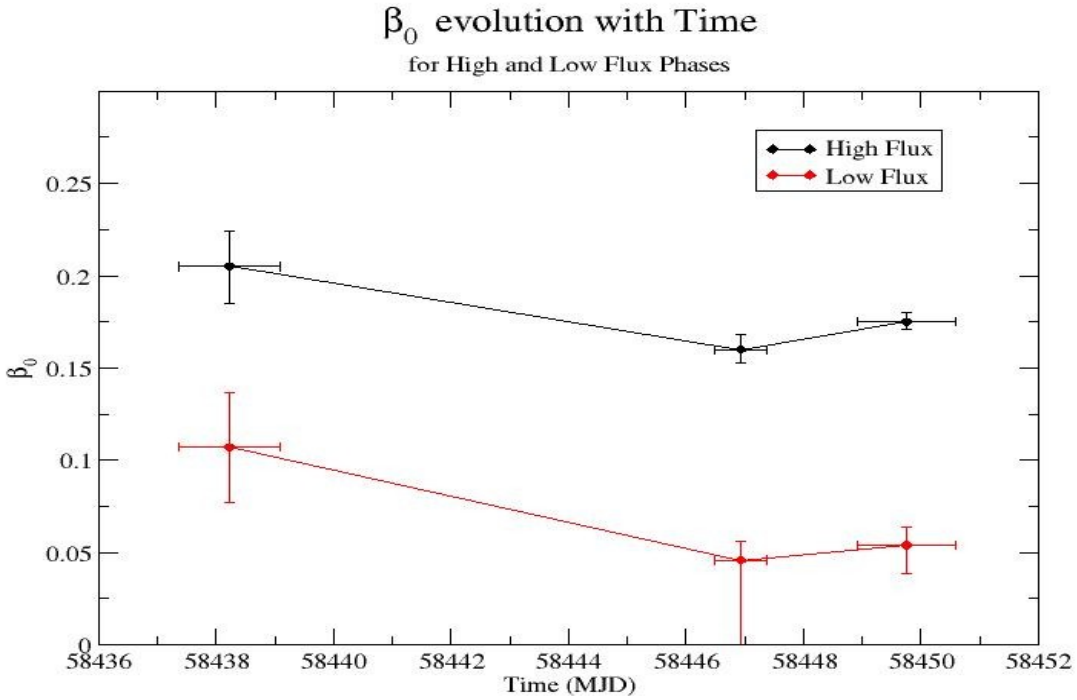

Figure 28: Terminal velocity of the accreting matter (in units of the speed of light) as a function of time, from Obs1 to Obs3 (the duration of each observation is represented by the error bars on the Time axis).

As we can see in these figures, the vertical optical depth decreases with increasing luminosity in both viewing angles (high flux and low flux). Note that the luminosity of the observations is gradually increasing (see Figure 11). The terminal velocity of the accreting gas is also decreasing, but it presents a small increase between Obs2 and Obs3. The electron temperature appears to increase from Obs1 to Obs2, but then it plateaus when the Obs3 was taking place. This is true only when viewing the accretion column from the side, as in the high flux view, we observe a decrease in kTe from Obs2 to Obs3.

These parameter behaviors could be explained by an increase in the accretion rate ($\dot{M}$), something that also explains the increase in luminosity we observe between the 3 observations. The higher $\dot{M}$ increases the radiation pressure inside the accretion column which, in turn, increases the height of the sonic surface. This leads to the increase in kTe, especially in the higher parts of the accretion column. As the density increases with the $\dot{M}$, the optical depth of the matter inside the column increases as well. Photons that could escape from the top, now find a smaller path when diffusing from the sides, so the ones left that we observe from the top, have a smaller vertical optical depth, hence the observed decrease in τ in Figure 26.

The luminosity is calculated by: $\boldsymbol{L = 4\pi f r^2}$, where ***f*** is the flux and ***r*** the distance to the object (~60.6 kpc) and in ***Table 4.2*** we can see its change between the 3 observations.

Table 4.2
Luminosity change of Swift J005139.2-721704

OBSERVATION ID	*Flux (10^{-10} erg/cm^2/s)*	*Luminosity (erg/s)*
30361003002	2.5769	$1.13 \cdot 10^{38}$
30361003004	3.8028	$1.67 \cdot 10^{38}$
30361003006	4.3357	$1.9 \cdot 10^{38}$

The Eddington (bolometric) Luminosity for pure Hydrogen is ~ $1.26 \cdot 10^{38} erg/sec$, so its value for our band (4 ~ 50 keV) is expected to be lower. By comparing it to the luminosities of the 3 observations, we conclude that SXP 4.78 is accreting at the super-Eddington limit.

4.2. Iron Line in Swift J005139.2-721704

Throughout our analysis of the NuSTAR data for Swift J005139.2-721704, we find that both the energy and the width (σ) of the Gaussian emission line feature are not entirely consistent with measurements of the FeKα line in other luminous accreting pulsars (e.g. Tendulkar et al., 2014). These values are typically ~ 6.3 keV and 0.1 keV respectively. In ***Table 4.3*** we can see the energy and σ values of the Gaussian component for Model ***[2]*** and Model ***[4]***.

Table 4.3
FeKα line energy and σ

OBSERVATION ID	*Model [2]*		*Model [4]*	
	Energy (keV)	***σ (keV)***	***Energy (keV)***	***σ (keV)***
30361003002	$6.2^{+0.2}_{-0.3}$	$1.0^{+0.3}_{-0.2}$	$5.933^{+0.2}_{-0.4}$	$1.3^{+0.2}_{-0.4}$
30361003004	$6.0^{+0.3}_{-0.6}$	$1.4^{+0.4}_{-0.3}$	$6.44^{+0.09}_{-0.1}$	$0.4^{+0.2}_{-0.4}$
30361003006	$5.8^{+0.3}_{-0.5}$	$1.6^{+0.4}_{-0.3}$	$6.527^{+0.2}_{-0.4}$	$0.27^{+0.07}_{-0.05}$

In Model ***[4]*** we can see that the energy appears to shift to higher energies, with the third (most luminous observation) having statistically significantly higher energy than the previous two observations. In the first observation, sigma is unrealistically large, but the other two are large but still consistent with each other.

The origin of the Iron emission line is from the accretion disk and, as expected, the phase-resolved-spectroscopy analysis presented no changes in the parameters of the Gaussian component. These facts lead us to believe that we might have a pulsar with a well developed accretion disk, so that the matter orbiting nearest to the neutron star is close enough to be irradiated by photons from the accretion column and produce a broad FeKα line.

4.3. Further Work

These results are very promising. In order to improve the quality of the constraints we can set on the physical parameters of the accretion flow we will combine the phase resolved spectra corresponding to phases of similar intensity. We will also further investigate the correlation between the different model parameters. Finally in order to set better constraints on the lower-energy part of the spectrum we will combine the NuSTAR data with data from the Neil Gehrels Swift Observatory, which has an energy range of 0.2 – 150 keV (Gehrels, 2004).

Chapter 5

Conclusions

In this thesis, we have presented the spectral analysis for the pulsar XTE 0052-723 (SXP 4.78), which is part of an HMXB system in the SMC. The data was acquired with the NuSTAR observatory in mid-November 2018. After performing the appropriate cleaning and calibration, we extracted spectra, which were then analyzed with XSPEC. The next step was to find a model that optimally fitted our data. We find that the data can be well represented by a phenomenological model consisting of a cutoff power-law a Gaussian emission line and photoelectric absorption. The photon index and energy of the cutoff are 1.22 - 1.26 and 5.2 – 11.7 keV respectively. The photon index does not present a change between the observations. The energy of the cutoff is decreasing, from 11.7^{+1}_{-1} in Obs1, to 9.2^{+2}_{-3} in Obs2 and 5.2^{+3}_{-2} in Obs3.

In order to obtain information on the physical conditions in the accretion column we also fitted the spectrum with the Becker and Wolff model (compmag). We find that a model consisting of commag, a Gaussian emission line and photoelectric absorptions gives a very good fit to the data. We find no evidence for a cyclotron resonant absorption feature (CRSF).

Chapter 6

References and Bibliography

Becker, P. and Wolff, M., 2007. Thermal and Bulk Comptonization in Accretion powered X-Ray Pulsars. *The Astrophysical Journal*, 654(1), pp.435-457.

Coe M. J., Kennea J. A., Buckley D., McBride V., Udalski A., Evans P., Roche P., Townsend L., 2018, The Astronomer's Telegram, 12229

Earth, Planets and Space, 2009. Call for Papers: Special Issue of Earth, Planets and Space (EPS) "International Geomagnetic Reference Fieldg—the eleventh generation". 61(4), pp.551-551.

Farinelli, R., Ceccobello, C., Romano, P. and Titarchuk, L., 2012. Numerical solution of the radiative transfer equation: X-ray spectral formation from cylindrical accretion onto a magnetized neutron star. *Astronomy & Astrophysics*, 538, p.A67.

Fiona A. Harrison *et al.*, 2013. The Nuclear Spectroscopic Telescope Array (NuSTAR) Mission. *The Astrophysical Journal*, 770, p.103.

Galloway, D., Giles, A., Wu, K. and Greenhill, J., 2001. Accretion column eclipses in the X-ray pulsars GX 1+4 and RX J0812.4-3114. *Monthly Notices of the Royal Astronomical Society*, 325(1), pp.419-425.

Gehrels, N. *et al.*, 2004. The Swift Gamma-Ray Burst Mission. *The Astrophysical Journal*, 611(2), pp. 1005-1020.

Guillot S., Vasilopoulos G., Pasham D., Jaisawal G. K., Ray P. S., Wolff M. T., Gendreau K. C., Strohmayer T. E., Arzoumanian Z., Corcoran M., Altamirano D., Wilson-Hodge C., Antoniou V., Zezas A., Haberl F., 2018, The Astronomer's Telegram, 12219

Haensel, P., Potekhin, A. and Yakovlev, D., 2007. *Neutron Stars 1*. New York, NY: Springer Science+Business Media, LLC.

Laycock, S., Corbet, R., Perrodin, D., Coe, M., Marshall, F. and Markwardt, C., 2002. Discovery of a new transient X-ray pulsar in the Small Magellanic Cloud. *Astronomy & Astrophysics*, 385(2), pp.464-470.

Mazzali, P., Ropke, F., Benetti, S. and Hillebrandt, W., 2007. A Common Explosion Mechanism for Type Ia Supernovae. *Science*, 315(5813), pp.825-828.

Monageng, I., Coe, M., Kennea, J., Townsend, L., Buckley, D., McBride, V., Udalski, A., Evans, P. and Roche, P., 2019. An X-ray and optical study of the outbursting behaviour of the SMC Be X-ray binary SXP 91.1. *Monthly Notices of the Royal Astronomical Society*, 489(1), pp.993-999.

Mushtukov, A., Suleimanov, V., Tsygankov, S. and Poutanen, J., 2015. The critical accretion luminosity for magnetized neutron stars. *Monthly Notices of the Royal Astronomical Society*, 447(2), pp.1847-1856.

Negueruela, I., Smith, D. M., Reig, P., Chaty, S., & Torrejn, J. M., 2006, *ESASP*, 604, p.165

Reig, P., 2011. Be/X-ray binaries. *Astrophysics and Space Science*, 332(1), pp.1-29.

Reisenegger A., 2001. Magnetic Fields of Neutron Stars: an Overview. Astrophysics (astro-ph), 0103010.

Rezzolla, L., Most, E. and Weih, L., 2018. Using Gravitational-wave Observations and Quasi-universal Relations to Constrain the Maximum Mass of Neutron Stars. *The Astrophysical Journal*, 852(2), p.L25.

Semena, A., Lutovinov, A., Mereminskiy, I., Tsygankov, S., Shtykovsky, A., Molkov, S. and Poutanen, J., 2019. Observational constraints on the magnetic field of the bright transient Be/X-ray pulsar SXP 4.78. *Monthly Notices of the Royal Astronomical Society*, 490(3), pp.3355-3364.

Struve, O., 1931. On the Origin of Bright Lines in Spectra of Stars of Class B. *The Astrophysical Journal*, 73, p.94.

Tanaka, Y. 1986, in Lecture Notes in Physics, Berlin Springer Verlag, Vol. 255, IAU Colloq. 89: Radiation Hydrodynamics in Stars and Compact Objects, ed. D. Mihalas & K.-H. A. Winkler, 198

Tendulkar, S., Fürst, F., Pottschmidt, K., Bachetti, M., Bhalerao, V., Boggs, S., Christensen, F., Craig, W., Hailey, C., Harrison, F., Stern, D., Tomsick, J., Walton, D. and Zhang, W., 2014. NuSTAR Discovery of a Cyclotron Line in the Be/X-Ray Binary RX J0520.5–6932 During Outburst. *The Astrophysical Journal*, 795(2), p.154.

West, B., Wolfram, K. and Becker, P., 2017. A New Two-fluid Radiation-hydrodynamical Model for X-Ray Pulsar Accretion Columns. *The Astrophysical Journal*, 835(2), p.129.

Wilms, J., Allen, A. and McCray, R., 2000. On the Absorption of X-Rays in the Interstellar Medium. *The Astrophysical Journal*, 542(2), pp.914-924.